

Scalable Equilibrium Sampling with Sequential Boltzmann Generators

Charlie B. Tan^{*1} Avishek Joey Bose^{*12} Chen Lin¹ Leon Klein³ Michael M. Bronstein¹ Alexander Tong²⁴

Abstract

Scalable sampling of molecular states in thermodynamic equilibrium is a long-standing challenge in statistical physics. Boltzmann generators tackle this problem by pairing powerful normalizing flows with importance sampling to obtain statistically independent samples under the target distribution. In this paper, we extend the Boltzmann generator framework and introduce SEQUENTIAL BOLTZMANN GENERATORS (SBG) with two key improvements. The first is a highly efficient non-equivariant Transformer-based normalizing flow operating directly on all-atom Cartesian coordinates. In contrast to equivariant continuous flows of prior methods, we leverage exactly invertible non-equivariant architectures which are highly efficient both during sample generation and likelihood computation. As a result, this unlocks more sophisticated inference strategies beyond standard importance sampling. More precisely, as a second key improvement we perform inference-time scaling of flow samples using annealed Langevin dynamics which transports samples toward the target distribution leading to lower variance (annealed) importance weights which enable higher fidelity resampling with sequential Monte Carlo. SBG achieves state-of-the-art performance w.r.t. all metrics on molecular systems, demonstrating the first equilibrium sampling in Cartesian coordinates of tri, tetra, and hexapeptides that were so far intractable for prior Boltzmann generators.

1. Introduction

The simulation of molecular systems at the all-atom resolution is of central interest in understanding complex natural processes. These include important biophysical processes

^{*}Equal contribution ¹University of Oxford ²Mila – Québec AI Institute ³Freie Universität Berlin ⁴Université de Montréal. Correspondence to: Charlie B. Tan <charlie.tan@cs.ox.ac.uk>, Avishek Joey Bose, Alexander Tong <bosejoey,alexander.tong@mila.quebec>.

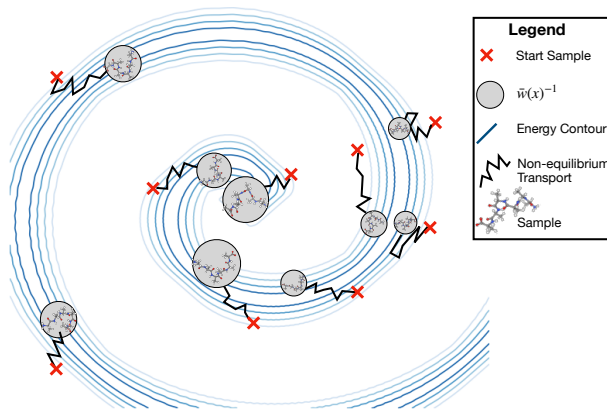


Figure 1. SBG uses inference time non-equilibrium transport to move initial proposal samples from a normalizing flow.

such as protein-folding (Noé et al., 2009; Lindorff-Larsen et al., 2011), protein-ligand binding (Buch et al., 2011), and formation of crystal structures (Parrinello & Rahman, 1980; Matsumoto et al., 2002), whose understanding can aid in problems that range from long-standing global health challenges to efficient energy storage (Deringer, 2020).

The dominant paradigm for molecular simulation involves running Markov Chain Monte Carlo (MCMC) or Molecular Dynamics (MD) whereby the equations of motion are integrated with finely discretized time steps. However, such molecular systems often exist in thermodynamic equilibrium by remaining for long time horizons in metastable states before rapidly transitioning to another metastable state. Such metastable states are captured in the minima of a complex energy landscape, associated with the molecular system’s equilibrium (Boltzmann) distribution at a given temperature. Unfortunately, drawing uncorrelated samples from such metastable states via traditional MD or MCMC methods is prohibitively computationally expensive, requiring long simulation steps with small updates on the order of femtoseconds $1\text{fs} = 10^{-15}\text{s}$, as transitions are rare events due to the presence of high-energy barriers between well-separated metastable states (Wirnsberger et al., 2020).

An alternative approach is to enhance sampling efficiency by leveraging powerful generative models such as normalizing flows (Dinh et al., 2017; Rezende & Mohamed, 2015)

trained on existing biased datasets, to produce approximate samples which can then be reweighted via importance sampling to follow the desired Boltzmann distribution. Such models, called *Boltzmann generators* (BG) (Noé et al., 2019), allow faster sampling through amortization as generation is significantly cheaper computationally than running MD or MCMC. Despite their appeal, it remains challenging for existing BGs to generate uncorrelated samples in their native Cartesian coordinates from the energy modes of the Boltzmann distribution for larger molecular systems at the scale of small peptides (2 amino acids) (Klein et al., 2023b; Midgley et al., 2023a). The principal drawback inhibiting scalability stems from the lack of expressive equivariant architectures that are also exactly invertible (Bose et al., 2021; Midgley et al., 2023a), or the present over-reliance on simple $E(n)$ -GNN’s (Satorras et al., 2021) based equivariant vector fields used in the design of continuous-time normalizing flows (Chen et al., 2018). As a result, even the most performant BGs suffer from low overlap with the target Boltzmann distribution, leading to poor sampling efficiency during importance sampling.

Table 1. Overview of the properties of models for sampling from target distributions with (possibly biased data).

Method	Use $\mathcal{E}(x)$	Exact Likelihoods	Use Data	Transport
DEM (Akhound-Sadeh et al., 2024)	✓	✗	✗	✗
NETS (Albergo & Vanden-Eijnden, 2024)	✓	✗	✗	✓
BG (Noé et al., 2019)	✓	✓	✓	✗
SBG (ours)	✓	✓	✓	✓

Present work. In this paper, we introduce SEQUENTIAL BOLTZMANN GENERATORS (SBG) a novel extension to the existing Boltzmann generator framework. SBG makes progress on the scalability of Boltzmann generators in Cartesian coordinates along two complementary axes: (1) scalable pre-training of softly SE(3)-equivariant proposal normalizing flows in BGs; and (2) inference time scaling of proposal flow samples and their importance weights under fast non-equilibrium processes, e.g. such as Langevin dynamics. The final result yields higher quality generated samples with reduced weight redundancy through SMC reweighting and thus allowing for the computation of important observable quantities such as free energy differences between metastable states of $\mu_{\text{target}}(x)$.

Our proposed approach SBG scales up proposal normalizing flows in BG’s by following recent advances in atomistic generative modeling, e.g. AlphaFold 3 (Abramson et al., 2024). In particular, we opt to remove the rigid SE(3)-equivariance as an explicit architectural inductive bias in favor of softly enforcing it through simpler and more efficient data augmentation. To further improve samples and their importance weights—a crucial step in the real-world application of BGs—we perform inference scaling by designing a target-informed non-equilibrium process. More precisely, we define an interpolation between the proposal

flow energy distribution (i.e., negative log density of samples) and the known target Boltzmann energy. Crucially, simulating samples at inference via the transport dynamics can be coupled to an equivalent time evolution of importance weights, converting naturally to the well-established technique of Sequential Monte Carlo (SMC) (Doucet et al., 2001) in continuous time. As a result, SBG can easily improve over the simple one-step importance sampling methodology used in existing BGs. We summarize the different aspects of our proposed SBG in comparison to other learned samplers and Boltzmann generators in Table 1.

We instantiate SBG using exactly invertible architectures by utilizing a modernized *non-equivariant* Transformer architecture as the backbone and use best-in-class models in TarFlow (Zhai et al., 2024). We demonstrate that exactly invertible architectures, because of fast and exact log-likelihood computations, benefit from inference-scaling. We emphasize this is in stark contrast to continuous normalizing flows that power prior SOTA Boltzmann generators which require both simulation of the 2nd order divergence operator and differentiating through an ODE solver. Furthermore, we demonstrate that enforcing equivariance softly along with appropriate normalization strategies enables us to stably scale the size of proposal flows in SBG. On a theoretical front, we study the added bias of common numerical tricks in the literature such as thresholding, and propose an automatic scheme to find the optimal thresholding parameter. Empirically, we observe SBG achieve state-of-the-art results across all metrics, and due to the enhanced computational efficiency far outperform continuous BG’s on all datasets. In particular, SBG is the first method to solve tripeptides, tetrapeptides, hexapeptides, and makes progress towards equilibrium sampling of decapeptides in Cartesian coordinates while past BG methods were intractable beyond dipeptides.

2. Background and preliminaries

We are interested in drawing statistically independent samples from the target Boltzmann distribution μ_{target} , with partition function \mathcal{Z} , defined over $\mathbb{R}^{n \times 3}$:

$$\mu_{\text{target}}(x) \propto \exp\left(\frac{-\mathcal{E}(x)}{k_B T}\right), \mathcal{Z} = \int_{\mathbb{R}^d} \exp\left(\frac{-\mathcal{E}(x)}{k_B T}\right) dx.$$

The Boltzmann distribution is defined for a system and includes the Boltzmann constant k_B , and is specified for a given temperature T . Additionally, the potential energy of the system $\mathcal{E} : \mathbb{R}^{n \times 3} \rightarrow \mathbb{R}$ and its gradient $\nabla \mathcal{E}$ can be evaluated at any point $x \in \mathbb{R}^{n \times 3}$, but the exact density $\mu_{\text{target}}(x)$ is not available as the partition function \mathcal{Z} associated to the Boltzmann distribution in general is intractable to evaluate.

In this paper, unlike pure sampling-based settings, we are afforded access to a small biased dataset of N samples

$\mathcal{D} = \{x^i\}_{i=1}^N$, provided as an empirical distribution $p_{\mathcal{D}}$. Consequently, it is possible to perform an initial learning phase that fits a generative model p_{θ} , with parameters θ , to $p_{\mathcal{D}}$ —e.g. by minimizing the forward KL $\mathbb{D}_{\text{KL}}(p_{\mathcal{D}}||p_{\theta})$ —to act as a proposal distribution that can be corrected.

2.1. Normalizing Flows

A key desirable property needed for the correction of a trained generative model p_{θ} on a biased dataset \mathcal{D} is the ability to extract an exact likelihood $p_{\theta}(x)$. Normalizing flows (Dinh et al., 2017; Rezende & Mohamed, 2015) represent exactly such a model class as they learn to transform an easy-to-sample base density to a desired target density using a parametrized diffeomorphism. More formally, given a sample from a (prior) base density $x_0 \sim p_0$ and a diffeomorphism $f_{\theta} : \mathbb{R}^{n \times 3} \rightarrow \mathbb{R}^{n \times 3}$ that maps the initial sample to $x_1 = f_{\theta}(x_0)$. We can obtain an expression for the log density of x_1 via the classical change of variables,

$$\log p_1(x_1) = \log p_0(x_0) - \log \det \left| \frac{\partial f_{\theta}(x_0)}{\partial x_0} \right|. \quad (1)$$

In Eq. 1 above the $\log \det |\cdot|$ term corresponds to the Jacobian determinant of f_{θ} evaluated at x_0 . Optimizing Eq. 1 is the maximum likelihood objective for training normalizing flows and results in f_{θ} learning $p_1 \approx p_{\text{data}}$. There are multiple ways to construct the (flow) map f_{θ} . Perhaps the most popular approach is to consider the flow to be a composition of a finite number of elementary diffeomorphisms $f_{\theta} = f_M \circ f_{M-1} \cdots \circ f_1$, resulting in the change in log density to be: $\log p_1(x_1) = \log p_0(x_0) - \sum_{i=1}^M \log |\partial f_{i,\theta}(x_{i-1}) / \partial x_{i-1}|$. We note that the construction of each $f_{i,\theta}, i \in [M]$ is motivated such that both the inverse $f_{i,\theta}^{-1}(x)$ and Jacobian $\partial f_{i,\theta}(x) / \partial x$ are computationally cheap to compute.

Continuous Normalizing Flows. In the limit of the infinite elementary diffeomorphisms, a normalizing transforms into a continuous normalizing flow (CNF) (Chen et al., 2018). Formally, a *flow* is a one-parameter time-dependent diffeomorphism $\psi_t : [0, 1] \times \mathbb{R}^{n \times 3} \rightarrow \mathbb{R}^{n \times 3}$ that is the solution to the following ordinary differential equation (ODE): $\frac{d}{dt} \psi_t(x) = u_t(\psi_t(x))$, with initial conditions $\psi_0(x_0) = x_0$, for a time-dependent vector field $u_t : [0, 1] \times \mathbb{R}^{n \times 3} \rightarrow \mathbb{R}^{n \times 3}$. It is often desirable to construct the target flow by associating it to a designated *probability path* $p_t : [0, 1] \times \mathbb{P}(\mathbb{R}^{n \times 3}) \rightarrow \mathbb{P}(\mathbb{R}^{n \times 3})$ which is a time-indexed interpolation in probability space between two distributions $p_0, p_1 \in \mathbb{P}(\mathbb{R}^{n \times 3})$. In such cases, the flow ψ_t is said to generate p_t if it pushes forward p_0 to p_1 by following u_t —i.e. $p_t = [\psi_t]_{\#}(p_0)$. As ψ_t is a valid flow and satisfies an ODE the change in log density can be computed using the instantaneous change of variables:

$$\log p(x_1) = \log p(x_0) - \int_0^1 \nabla \cdot u_t(x_t) dt, \quad (2)$$

where $x_t = \psi_t(x_0)$ and $\nabla \cdot$ is the divergence operator.

A CNF can then be viewed as a neural flow that seeks to learn a designated target flow ψ_t for all time $t \in [0, 1]$. The most scalable way to train CNFs is to employ a flow-matching learning framework (Liu, 2022; Albergo & Vanden-Eijnden, 2023; Lipman et al., 2023; Tong et al., 2023). Specifically, flow-matching regresses a learnable vector field of a CNF $f_{t,\theta}(t, \cdot) : [0, 1] \times \mathbb{R}^{n \times 3} \rightarrow \mathbb{R}^{n \times 3}$ to the target vector field $u_t(x_t)$ associated to the flow ψ_t . In practice, it is considerably easier to regress against a target *conditional* vector field $u_t(x_t|z)$ —which generates the conditional probability path $p_t(x_t|z)$ —as we do not have closed form access to the (marginal) vector field u_t which generates p_t . The conditional flow-matching (CFM) objective can then be stated as a simple simulation-free regression,

$$\mathcal{L}_{\text{CFM}}(\theta) = \mathbb{E}_{t,q(z),p_t(x_t|z)} \|f_{t,\theta}(t, x_t) - u_t(x_t|z)\|_2^2. \quad (3)$$

The conditioning distribution $q(z)$ can be chosen from any valid coupling, for instance, the independent coupling $q(z) = p(x_0)p(x_1)$. We highlight that Eq. 3 allows for greater flexibility in $f_{t,\theta}$ as there is no exact invertibility constraint. To generate samples and their corresponding log density according to the CNF we may solve the following flow ODE numerically with initial conditions $x_0 = \psi_0(x_0)$ and $c = \log p_0(x_0)$, which is the log density under the prior:

$$\frac{d}{dt} \begin{bmatrix} \psi_{t,\theta}(x_t) \\ \log p_t(x_t) \end{bmatrix} = \begin{bmatrix} f_{t,\theta}(t, x_t) \\ -\nabla \cdot f_{t,\theta}(t, x_t) \end{bmatrix}. \quad (4)$$

2.2. Boltzmann generators

A Boltzmann generator (Noé et al., 2019) μ_{θ} pairs a normalizing flow as the proposal generative model p_{θ} , which is then corrected to obtain i.i.d. samples under μ_{target} using importance sampling. More precisely, as normalizing flows are exact likelihood models, BG’s first draw K independent samples $x^i \sim p_{\theta}(x), i \in [K]$ and compute the corresponding importance weights for each sample $w(x^i) = \exp\left(\frac{-\mathcal{E}(x^i)}{k_B T}\right) / p_{\theta}(x^i)$. Leveraging the collection of importance weights we can compute a Monte-Carlo approximation to any test function $\phi(x)$ of interest under μ_{target} using self-normalized importance sampling as follows:

$$\mathbb{E}_{\mu_{\text{target}}(x)}[\phi(x)] = \mathbb{E}_{p_{\theta}}[\phi(x)\bar{w}(x)] \approx \frac{\sum_{i=1}^K w(x^i)\phi(x^i)}{\sum_{i=1}^K w(x^i)}.$$

In addition, computing importance weights also enables resampling the pool of samples according to the collection of normalized importance weights $W = \{\bar{w}(x^i)\}_{i=1}^K$.

3. SEQUENTIAL BOLTZMANN GENERATORS

We now present SBG which extends and improves over classical Boltzmann generators by adding a non-equilibrium

sampling process that leads to higher-quality samples with reduced redundancy. We begin by identifying the key limitation in current BG’s as importance sampling with a suboptimal proposal. Indeed, while the self-normalized importance sampling estimator is consistent, its’ fidelity is highly dependent on the quality of the actual proposal p_θ . In fact, the optimal proposal distribution is proportional to the minimizer of the variance of $\phi(x^i)\mu_{\text{target}}(x^i)$ (Owen, 2013). Unfortunately, since p_θ within a BG framework is trained on a biased dataset \mathcal{D} the importance weights computed typically exhibit large variance—resulting in a small effective sample size (ESS).¹

We address the need for more flexible proposals in §3.1 with modernized scalable training recipes for normalizing flows. In §3.2 we outline our novel application of non-equilibrium sampling with Sequential Monte Carlo (Doucet et al., 2001) that powers our inference scaling algorithm to transport proposal samples and their importance weight towards the metastable states of $\mathcal{E}(x)$. We term the overall process of combining a pre-trained Boltzmann generator with inference scaling through annealing: SEQUENTIAL BOLTZMANN GENERATORS.

Symmetries of molecular systems. The energy function $\mathcal{E}(x)$ in a molecular system using classical force fields is known to be invariant under global rotations and translation², which corresponds to the group $\text{SE}(3) \cong \text{SO}(3) \ltimes (\mathbb{R}^3, +)$. Unfortunately, $\text{SE}(3)$ is a non-compact group which does not allow for defining a prior density $p_0(x_0)$ on $\mathbb{R}^{n \times 3}$. Equivariant generative models circumvent this issue by defining a mean-free prior which is a projection of a Gaussian prior $\mathcal{N}(0, I)$ onto the subspace $\mathbb{R}^{(n-1) \times 3}$ (Garcia Satorras et al., 2021). Thus pushing forward a mean free prior with an equivariant flow provably leads to an invariant proposal $p_1(x_1)$ (Köhler et al., 2020; Bose et al., 2021). We next build BG’s by departing from exactly equivariant maps by instead considering soft-equivariance which opens up the usage of more scalable and efficient architectures.

3.1. Scaling training of Boltzmann generators

To improve proposal flows in SBG we favor scalable architectural choices that are more expressive than exactly equivariant ones. We motivate this choice by highlighting that many classes of normalizing flow models are known to be universal density approximators (Teshima et al., 2020; Lee et al., 2021). Thus, expressive enough non-equivariant flows *can learn to approximate any equivariant map*.

Soft equivariance. We instantiate SBG with a state-of-the-art TarFlow (Zhai et al., 2024) which is based on Blockwise

¹ESS is defined as: $\text{ESS} = 1 / \sum_i^K (\bar{w}(x^i))^2$.

²In classical force fields, in contrast to semi-empirical ones, the correct ordering of the topology is needed for energy evaluation.

Masked Autoregressive Flow (Papamakarios et al., 2017) based on a causal Vision Transformer (ViT) (Alexey, 2021) modified for molecular systems where patches are over the particle dimension. Since the data comes mean-free we further normalize the data to a standard deviation of one. Combined, this allows us to scale both the depth and width of the models stably as there is no tension between a hard equivariance constraint and the invertibility of the network.

We include a series of strategies to improve training of non-equivariant flows by softly enforcing $\text{SE}(3)$ -equivariance. First, we softly enforce equivariance to global rotations through data augmentation by sampling random rotations $R \in \text{SO}(3)$ and applying them to data samples $R \circ x_1 \sim p_1(x_1)$. Secondly, as the data is mean-free and has $(n-1) \times d$ degrees of freedom we lift the data dimensionality back to n by adding noise to the center of mass. This allows us to easily train with a non-equivariant prior distribution such as the standard normal $p_0 = \mathcal{N}(0, I)$. The next proposition outlines the family of permissible noise.

Proposition 1. *Given an $\text{SE}(3)$ -invariant $\mu_{\text{target}}(x)$ and the noise-adjusted distribution $\mu'_{\text{target}}(x)$. Consider the decomposition of a data sample into its constituent mean-free component, \tilde{x} and center of mass $c \in \mathbb{R}^3$, $x = \tilde{x} + c$, where $c \sim \mu(c)$ and $\mu(c)$ is $\text{SO}(3)$ -invariant. Then $\mu_{\text{target}}(\tilde{x}) = \mu'_{\text{target}}(\tilde{x})$ if $\mu'_{\text{target}}(x) = \mu(\tilde{x})\mu(\|c\|)$.*

We prove Proposition 1 in §B.1, which tells us that any noise distribution that acts on the norm of the center of mass does not operationally change the target. As a result, we choose to add small amounts of Gaussian noise $c \sim \mathcal{N}(0, \sigma)$ to the center of mass of a given data sample. The impact of this noise is that during reweighting we must account for $\mu(\|c\|)$ which follows a $\chi(3)$ distribution. Consequently, we must adjust the model energy to account for the impact of CoM noise during reweighting as follows:

$$\log p_\theta^c(x) = \log p_\theta(x) - \left(\log \left(\frac{\|c\|^2}{\sigma^3} \right) + \frac{\|c\|^2}{2\sigma^2} + C \right), \quad (5)$$

where $C = -\log(\sqrt{2}\Gamma(\frac{3}{2}))$ and Γ is the gamma function.

3.2. Inference time scaling of Boltzmann generators

Given a trained BG with proposal flow p_θ , the simple importance sampling estimator suffers from a large variance of importance weights as the dimensionality and complexity of $\mu_{\text{target}}(x)$ grows in large molecular systems. We aim to address this bottleneck by proposing an inference time scaling algorithm that anneals samples $x^i \sim p_\theta(x)$ —and corresponding unnormalized importance weights $w(x^i)$ —in a continuous manner towards μ_{target} .

Improving samples through non-equilibrium transport. We leverage a class of methods that fall under

non-equilibrium sampling to improve the base proposal flow samples. One of the simplest instantiations of this idea is to use annealed Langevin dynamics with reweighting through a continuous-time variant of Annealed Importance Sampling (AIS) (Neal, 2001). Concretely, we consider the following SDE that drives proposal samples towards metastable states of the Boltzmann target:

$$dx_\tau = -\epsilon_\tau \nabla \mathcal{E}_\tau(x_\tau) d\tau + \sqrt{2\epsilon_\tau} dW_\tau, \quad (6)$$

where $\epsilon_\tau \geq 0$ is a time-dependent diffusion coefficient and W_τ is the standard Wiener process. We distinguish τ , from t used in the context of training p_θ , as the time variable that evolves initial proposal samples at $\tau = 0$ towards the target at $\tau = 1$. The energy interpolation \mathcal{E}_t is a design choice, and we opt for a simple linear interpolant $\mathcal{E}_t = (1 - \tau)\mathcal{E}_0 + \tau\mathcal{E}_1$, and set $\mathcal{E}_0(x) = -\log p_\theta(x)$. We highlight that unlike past work in pure sampling (Máté & Fleuret, 2023; Albergo & Vanden-Eijnden, 2024) which use the prior energy $\mathcal{E}_0(x) = -\log p_0(x)$, our design affords the significantly more informative proposal given by the pre-trained normalizing flow p_θ . As such, there is often no need for *additional learning* during this step which we view as extending the inference capabilities of the original Boltzmann generator $\mu_\theta(x)$.

To compute test functions for the transported samples, and thus reweighting, we use a well-known and celebrated result known as Jarzynski’s equality that enables the calculation of equilibrium statistics from non-equilibrium processes. We recall the main result, originally derived in Jarzynski (1997), and recently re-derived in continuous-time in the context of learning to sample by Vargas et al. (2024); Albergo & Vanden-Eijnden (2024) that makes explicit the time evolution of the new importance weights.

Proposition 2 (Albergo & Vanden-Eijnden (2024)). *Let (x_τ, w_τ) solve the coupled system of SDE / ODE*

$$\begin{aligned} dx_\tau &= -\epsilon_\tau \nabla \mathcal{E}_\tau(x_\tau) d\tau + \sqrt{2\epsilon_\tau} dW_\tau \\ d \log w_\tau &= -\partial_\tau \mathcal{E}_\tau(x_\tau) d\tau \quad \text{with } x_0 \sim p_\theta, w_0 = 0 \end{aligned}$$

then for any test function $\phi : \mathbb{R}^d \rightarrow \mathbb{R}$ we have

$$\int_{\mathbb{R}^d} \phi(x) p_\tau(x) dx = \frac{\mathbb{E}[w_\tau \phi(x_\tau)]}{\mathbb{E}[w_\tau]} \quad (7)$$

and

$$\mathcal{Z}_\tau / \mathcal{Z}_1 = \mathbb{E}[e^{w_\tau}] \quad (\text{Jarzynski’s Equality}) \quad (8)$$

The final samples $x_{\tau=1}$ can then be reweighted according to final importance weights $w_{\tau=1}$ that have lower variance than simple importance sampling in conventional BGs. It is crucial to highlight that through inference-time scaling, we never need to utilize the high-variance importance weights under the prior $p_0(x_0)$, and instead the proposal $p_\theta(x_0)$

acts as a new prior for the annealing process. It is precisely this learned proposal distribution that $d \log w_\tau$ accounts for within the parlance of Annealed Importance Sampling. To evolve the Langevin SDE we require,

$$\nabla \mathcal{E}_\tau(x_\tau) = (1 - \tau) \nabla (-\log p_\theta(x_\tau)) + \tau \nabla \left(\frac{\mathcal{E}(x_\tau)}{k_B T} \right),$$

which requires efficient gradient computation through the log-likelihood estimation under the normalizing flow p_θ as given by Eq. 1. This presents the first point of distinction between finite flows and CNF’s. The former class of flows trained using Eq. 1 gives fast exact likelihoods—especially for our scalable non-equivariant TarFlow model. In contrast, CNF’s must simulate Eq. 4 and differentiate through an ODE solver to compute $\nabla \log p_\theta(x_\tau)$ for each step of the Langevin SDE in Eq. 6. As a result, a TarFlow proposal is considerably cheaper to simulate and reweight with AIS than a CNF. In §A we present an alternate interpolant that does not require the proposal distribution during sampling which is appealing when only samples are needed but at the cost of more expensive computation of log weights. These paths are of interest in the setting of Boltzmann emulators and other generative models and are of independent interest but are not considered further in the context of SBG.

To further enable a reduced computational footprint we propose a strategy that eliminates the forward evolution of the initial proposal that already obtain high energy. Specifically, we can simulate a large number of samples via Eq. 11 and threshold using an energy threshold $\gamma > 0$, and evaluate the log weights of promising samples. We justify our strategy by first remarking a lower bound to the log partition function of μ_{target} using a Monte Carlo estimate,

$$\begin{aligned} \log \mathcal{Z} &= \log \mathbb{E}_{x \sim p_\theta(x)} \left[\frac{\exp \left(\frac{-\mathcal{E}(x)}{k_B T} \right)}{p_\theta(x)} \right] \\ &\geq \mathbb{E}_{x \sim p_\theta(x)} \left[\frac{-\mathcal{E}(x)}{k_B T} - \log p_\theta(x) \right] = \log \hat{\mathcal{Z}}. \quad (9) \end{aligned}$$

Plugging this estimate in the definition of the target Boltzmann distribution we get an upper bound,

$$\log \mu_{\text{target}}(x) \leq \log \left(\frac{-\mathcal{E}(x)}{k_B T} \right) - \log \hat{\mathcal{Z}}.$$

An upper bound on $\mu_{\text{target}}(x)$ allows us to threshold samples using the energy function, $\mathcal{E}(x) > \gamma$, of the target. Formally, this corresponds to truncating the target distribution $\hat{\mu}_{\text{target}}(x) := \mathbb{P} \left(\mu_{\text{target}}(x) \geq \frac{\gamma}{\log \hat{\mathcal{Z}}} \right)$ which places zero mass on high energy conformations. Correcting flow samples with respect to this truncated target introduces an additional bias into the self-normalized importance sampling estimate, which precisely corresponds to the

difference in total variation distance between the two distributions $\text{TV}(\hat{\mu}_{\text{target}}, \mu_{\text{target}})$. We prove this result using an intermediate result in Lemma 1 included in Appendix B.

Our next theoretical result provides a prescriptive strategy of setting an appropriate threshold γ as a function of the number of samples K and effective sample size under $\hat{\mu}_{\text{target}}(x)$.

Proposition 3. *Given an energy threshold $\mathcal{E}(x) > \gamma$, for $\gamma > 0$ large and the resulting truncated target distribution $\hat{\mu}_{\text{target}}(x) := \mathbb{P}\left(\mu_{\text{target}}(x) \geq \frac{\gamma}{\log \hat{\mathcal{Z}}}\right)$. Further, assume that the density of unnormalized importance weights w.r.t. to $\hat{\mu}_{\text{target}}$ is square integrable $(\hat{w}(x))^2 < \infty$. Given a tolerance $\rho = 1/\text{ESS}$ and bias of the original importance sampling estimator in total variation $b = \text{TV}(\mu_\theta, \mu_{\text{target}})$, then the γ -truncation threshold with K -samples for $\text{TV}(\mu_\theta, \hat{\mu}_{\text{target}})$ is:*

$$\gamma \geq \frac{1}{\lambda} \log \left(\frac{Kb}{12\rho\mathbb{E}[\exp(-\lambda X)]} \right) + \log \hat{\mathcal{Z}}. \quad (10)$$

The proof for Proposition 3 is located in §B.3. Proposition 3 allows us to appropriately set a energy threshold γ as a function of tolerance ρ that depends on ESS. In practice, this allows us to negotiate the amount of acceptable bias when dropping initial samples that obtain high-energy before any further AIS correction. Moreover, this gives a firmer theoretical foundation to existing practices of thresholding high-energy samples (Midgley et al., 2023b;a).

Analogous to thresholding based on $\mathcal{E}(x)$, we can also threshold by the probability under the proposal flow with truncation $\hat{p}_\theta(x) := \mathbb{P}(p_\theta(x) \geq \delta)$, for small $\delta > 0$. Essentially, this thresholding filters low probability samples under the model prior to any importance sampling. The additional bias incurred by performing such thresholding is theoretically analyzed in Proposition 4 and presented in §B.4.

Algorithm 1 SBG Sampling

Require: # particles K , # annealed distributions N , Energy annealing schedule $\mathcal{E}_\tau(x_\tau)$

- 1: $x_0 \sim \mathcal{E}_0(x_0)$; $\Delta \leftarrow 1/N$
- 2: **for** $i = 1$ to N **do**
- 3: $x_{\tau+\Delta} \leftarrow x_\tau - \epsilon_\tau \nabla \mathcal{E}_\tau(x_\tau) d\tau + \sqrt{2\epsilon_\tau} dW_\tau$
- 4: $\log w_{\tau+\Delta} \leftarrow \log w_\tau - \partial_\tau \mathcal{E}_\tau(x_\tau) d\tau$
- 5: $\tau \leftarrow \tau + \Delta$
- 6: **if** $\text{ESS} < \text{ESS}_{\text{threshold}}$ **then**
- 7: $x_\tau \leftarrow \text{RESAMPLE}(x_\tau, w_\tau)$
- 8: $w_\tau \leftarrow 0$
- 9: **end if**
- 10: **end for**

4. Experiments

We evaluate SBG on small peptides using classical force-fields as the energy function with exact experimental setups described in §E. To generate samples and their corresponding weights we follow Algorithm 1 with resampling (lines 6-9) which is run on initial proposal samples and is equivalent to performing SMC (Doucet et al., 2001).

Datasets. We consider small peptides composed of varying numbers of alanine amino acids, with some systems additionally incorporating an acetyl group and an N-methyl group. We investigate alanine systems of up to 6 amino acids. All datasets are generated from a single MD simulation in implicit solvent using a classical force field. For each system, the first 100ps is used for training, the next 20ps for validation, and the remainder serves as the test set. Therefore, some metastable states may not be represented in the training set. An exception is alanine dipeptide, for which we use the dataset from Klein & Noé (2024). In addition to the alanine systems, we also investigate the significantly larger protein Chignolin, consisting of 10 amino acids generated with the Anton supercomputer in Lindorff-Larsen et al. (2011). We provide additional dataset details in §D.

Baselines. For baselines, we train prior state-of-the-art equivariant Boltzmann generators. Specifically, we use SE(3)-augmented coupling flow (Midgley et al., 2023a) as the exactly invertible and equivariant architecture and the equivariant ECNF employed in Transferrable Boltzmann Generators (Klein & Noé, 2024). We also include an improved equivariant CNF (ECNF++) as a stronger baseline, see §E.3 for full details, which uses improved flow matching loss, improved data normalization, a larger network, improved learning rate schedule, and optimizer. We note that ECNF is equivariant to E(3) and hence generates samples of both global chiralities, which we resolve by applying a flip transformation as in Klein & Noé (2024), for further details see §F.

Metrics. We report interatomic distances as a normalized density between the ground truth data, and initial proposal samples, as well as the energy histogram of the system for ground truth, initial proposal samples, transported samples, and the reweighted energy histogram. We also include Ramachandran plots (Ramachandran et al., 1963) for each molecular system studied that visualizes dihedral angles’ distribution for the ground truth data distribution and the generated samples. We include additional quantitative metrics that provide a finer grained evaluation of each method. Concretely, we compute the ESS, Wasserstein-1 distance on the energy distribution, and the Wasserstein-2 distance of the dihedral angles used in the Ramachandran plot.

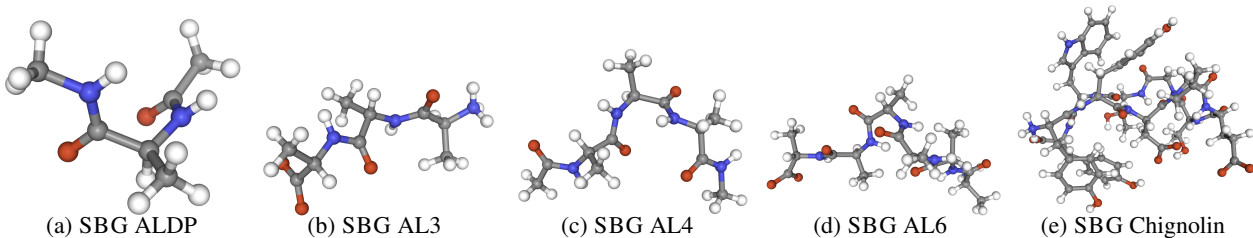


Figure 2. Generated samples from SBG on molecular systems ranging from 2 to 10 amino acids.

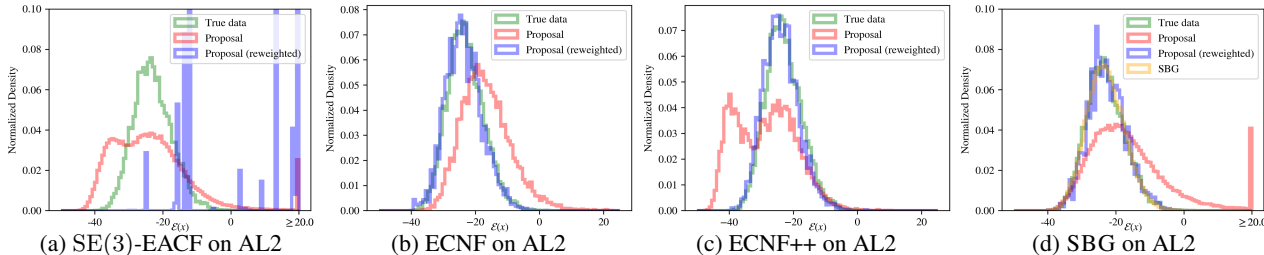


Figure 3. Energies of samples generated with different methods on alanine dipeptide (ALDP).

4.1. Results

We evaluate SBG and our chosen baselines on alanine dipeptide (ALDP), trialanine (AL3), alanine tetrapeptide (AL4), and hexaalanine (AL6) with quantitative metrics summarized in Table 2 and Table 3 and generated samples in Figure 2. In SBG @ 10k we generate 10k samples and directly report metrics on these samples. In SBG @ 100k we generate 100k samples and subsample to 10k after SMC to compute directly comparable metrics. For SE(3)-EACF we retrain this baseline on our more challenging version of ALDP and observe that performance degrades substantially at the selected 0.2% weight clipping threshold (c.f. §F for higher clipping thresholds). Furthermore, we find that on ALDP, our improved ECNF++ baseline obtains a 177% relative improvement in ESS over the previous SOTA ECNF from Klein & Noé (2024). Importantly, we observe SBG is the best method on the Wasserstein-1 energy distance $\mathcal{E}\text{-}\mathcal{W}_1$ and Wasserstein-2 distance on dihedral angles $\mathbb{T}\text{-}\mathcal{W}_2$. As SBG involves resamples on a finite set of points, we observe that the higher number of particles (100k) results in consistently improved $\mathcal{E}\text{-}\mathcal{W}_1$ and $\mathbb{T}\text{-}\mathcal{W}_2$. These results are further substantiated in Figure 3 which depicts the energy histograms of SBG in relation to the ground truth energy of the system and depicts a near perfect overlap.

For tripeptides, tetrapeptides, and hexapeptides we remark that the SE(3)-EACF baseline is too computationally expensive and thus does not scale (c.f. Table 5). Consequently, we report metrics for our improved ECNF, ECNF++, and SBG. We observe that ECNF fails to learn effectively on the tri and tetrapeptides with $\mathcal{E}\text{-}\mathcal{W}_1$ exploding over 10^4 , while our improved ECNF++ is orders of magnitude better. We highlight that SBG is the best method across all metrics, and

in particular, we highlight that the improvements are more prominently driven by inference time scaling of proposal samples as observed in Figure 5, Figure 6, and Figure 7. As reweighted samples under SBG show extremely high overlap with the ground truth $\mu_{\text{target}}(x)$, we argue that SBG successfully solves these molecular systems in comparison to prior BG’s. We also report in §F.2 the Ramachandran plots for each method. Finally, we include additional ablations such as the utility of CoM energy adjustment in Appendix F.

Inference scaling. To illustrate the scalability of SBG in relation to other methods we plot in Figure 4 the log-scale inference time for each dataset. In particular, for inference, we include the time to generate and reweight $10k$ samples. We observe an almost exponential scaling of ECNF as the size of the peptide grows, while SBG is dramatically faster at inference. We also plot $\mathbb{T}\text{-}\mathcal{W}_2$ metric on AL3 as a function of Langevin timestep granularity which shows a monotonic decrease as the number of samples increase for the center of mass adjusted energy, demonstrating a dimension for inference-time scaling of SBG not present in standard Boltzmann generators. Furthermore, the standard energy function does not give monotonic improvement with increasing granularity, demonstrating the improvement achieved by the center of mass adjusted energy.

Table 2. Quantitative results on ALDP. * Indicates resampled ESS.

Datasets →	Alanine dipeptide (ALDP)		
	ESS ↑	$\mathcal{E}\text{-}\mathcal{W}_1$ ↓	$\mathbb{T}\text{-}\mathcal{W}_2$ ↓
Algorithm ↓			
SE(3)-EACF	$< 10^{-4}$	3.31	2.92
ECNF	0.084	0.984	0.391
ECNF++ (Ours)	0.260 ± 0.043	0.796 ± 0.081	0.293 ± 0.017
SBG (Ours) @ 10k	$0.897^* \pm 0.167$	0.536 ± 0.367	0.502 ± 0.108
SBG (Ours) @ 100k	$0.894^* \pm 0.172$	0.466 ± 0.380	0.226 ± 0.029

Table 3. Quantitative results on trialanine, alanine tetrapeptide, and hexapeptide. *Indicates ESS after resampling.

Datasets →	Tripeptide (AL3)			Tetrapeptide (AL4)			Hexapeptide (AL6)		
Algorithm ↓	ESS ↑	$\mathcal{E}\text{-}\mathcal{W}_1$ ↓	$\mathbb{T}\text{-}\mathcal{W}_2$ ↓	ESS ↑	$\mathcal{E}\text{-}\mathcal{W}_1$ ↓	$\mathbb{T}\text{-}\mathcal{W}_2$ ↓	ESS ↑	$\mathcal{E}\text{-}\mathcal{W}_1$ ↓	$\mathbb{T}\text{-}\mathcal{W}_2$ ↓
ECNF	$< 10^{-4}$	$> 10^4$	4.241	$< 10^{-4}$	$> 10^4$	4.902	-	-	-
ECNF++ (Ours)	0.036 ± 0.027	1.759 ± 0.788	1.177 ± 0.145	0.123 ± 0.006	4.229 ± 1.284	2.082 ± 0.005	0.015	8.954	4.315
SBG (Ours) @10k	$0.876^* \pm 0.215$	1.456 ± 0.739	1.303 ± 0.039	$0.901^* \pm 0.059$	1.517 ± 0.387	2.080 ± 0.028	0.995^*	2.321	3.697
SBG (Ours) @100k	$0.907^* \pm 0.151$	1.314 ± 0.409	0.948 ± 0.068	$0.886^* \pm 0.087$	1.920 ± 0.251	1.841 ± 0.047	0.989^*	0.305	3.326

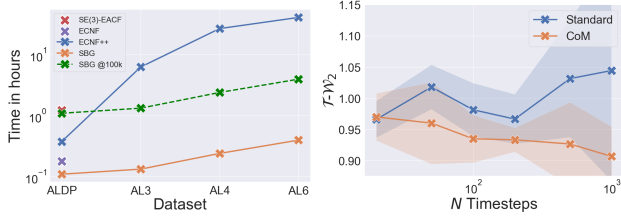
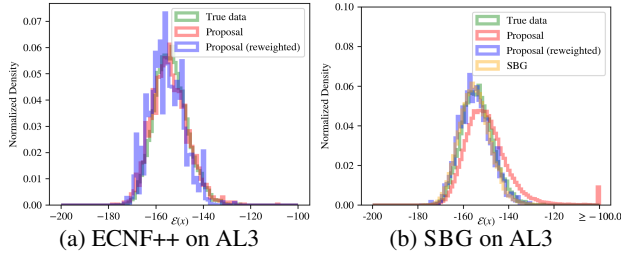

 Figure 4. **Left:** Time in hours for sampling and reweighting 10k points. **Right:** $\mathbb{T}\text{-}\mathcal{W}_2$ on AL3 as a function of Langevin timestep granularity for both standard and center of mass adjusted proposal energy functions.


Figure 5. Energy plots for trialanine (AL3).

4.2. Scaling to decapeptides

We now apply SBG to a decapeptide in Chignolin. As no other baseline can scale to this molecule we report energy histograms and distance plots for SBG only in Figure 8. We observe success of SBG at matching the interatomic distance distribution. We additionally observe imperfect but reasonable proposal samples under the energy distribution whose energies are greatly improved after reweighting. Evidently the equilibrium distribution is not perfectly sampled as evidenced by the lack of density at the lowest energy states and large peaks in the reweighted distributions. Nevertheless, our application of SBG to Chignolin represents a significant step towards the scalability of BG’s that previously struggled on even tripeptides like AL3 as found in the ECNF $\mathcal{E}\text{-}\mathcal{W}_1$ result in Table 3.

5. Related work

Boltzmann generators (BGs) (Noé et al., 2019) have been applied to both free energy estimation (Wirnsberger et al., 2020; Rizzi et al., 2023; Schebek et al., 2024) and molecular sampling. Initially, BGs relied on system-specific

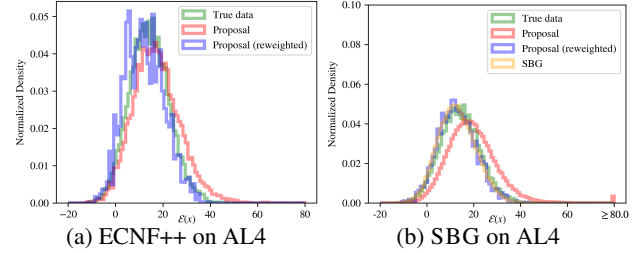


Figure 6. Energy plots for tetrapeptide (AL4).

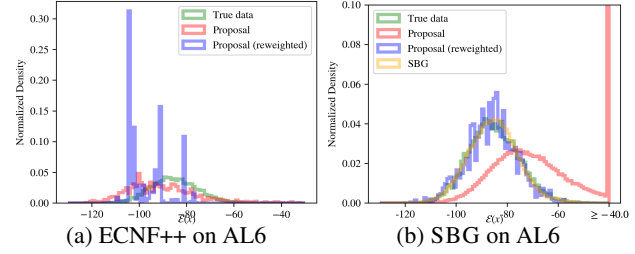


Figure 7. Energy plots for hexapeptide (AL6).

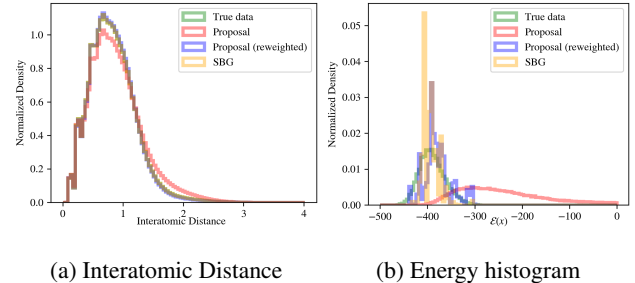


Figure 8. Interatomic distance and energy plots for Chignolin.

representations, such as internal coordinates, to achieve relevant sampling efficiencies (Noé et al., 2019; Köhler et al., 2021; Midgley et al., 2023b; Köhler et al., 2023; Dibak et al., 2022). However, these representations are generally not transferable across different systems, leading to the development of BGs in Cartesian coordinates (Klein et al., 2023b; Midgley et al., 2023a; Klein & Noé, 2024). While this improves transferability, they are currently limited in scalability, struggling to extend beyond dipeptides. Scaling to larger systems typically requires sacrificing exact sampling from the target distribution (Jing et al., 2022; Abdin & Kim, 2023; Jing et al., 2024a; Lewis et al., 2024), which often includes coarse-graining. An alternative to direct sampling from $\mu_{\text{target}}(x)$ is to

generate samples iteratively by learning large steps in time (Schreiner et al., 2023; Fu et al., 2023; Klein et al., 2023a; Diez et al., 2024; Jing et al., 2024b; Daigavane et al., 2024).

6. Conclusion

In this paper, we introduce SBG an extension to the Boltzmann generator framework that scales inference through the use of non-equilibrium transport. Unlike past BG’s in SBG, we scale training using a non-equivariant transformer-based TarFlow architecture with soft equivariance penalties to 6 peptides. In terms of limitations, using non-equilibrium sampling as presented in SBG does not enjoy easy application to CNFs due to expensive simulation, which limits the use of modern flow matching methods in a SBG context. Considering hybrid approaches that mix CNFs through distillation to an invertible architecture or consistency-based objectives is thus a natural direction for future work. Finally, considering other classes of scalable generative models such as autoregressive ones which also permit exact likelihoods is also a ripe direction for future work.

7. Impact Statement

This work studies amortized sampling from Boltzmann densities, a problem of general interest in machine learning and AI4Science that arises both in pure statistical modeling and in applications. We highlight the training Boltzmann generators on molecular tasks are in turn applicable to drug and material discovery. While we do not foresee immediate negative impacts of our advances in this area, we encourage due caution when scaling up to prevent their potential misuse.

Acknowledgements

The authors would like to thank Tara Akhound-Sadegh, Lars Holdijk, Kacper Kapuśniak, Kirill Neklyodov, and Michael Albergo for useful conversations and feedback on this work.

The authors acknowledge funding from UNIQUE, CIFAR, NSERC, Intel, and Samsung. The research was enabled in part by computational resources provided by the Digital Research Alliance of Canada (<https://alliancecan.ca>), Mila (<https://mila.quebec>), and NVIDIA. AJB is partially supported by an NSERC Post-doc fellowship. This research is partially supported by EPSRC Turing AI World-Leading Research Fellowship No. EP/X040062/1 and EPSRC AI Hub on Mathematical Foundations of Intelligence: An “Erlangen Programme” for AI No. EP/Y028872/1

References

- Abdin, O. and Kim, P. M. Pepflow: direct conformational sampling from peptide energy landscapes through hypernetwork-conditioned diffusion. *bioRxiv*, pp. 2023–06, 2023. (Cited on page 8)
- Abramson, J., Adler, J., Dunger, J., Evans, R., Green, T., Pritzel, A., Ronneberger, O., Willmore, L., Ballard, A. J., Bambrick, J., et al. Accurate structure prediction of biomolecular interactions with alphafold 3. *Nature*, pp. 1–3, 2024. (Cited on page 2)
- Agapiou, S., Papaspiliopoulos, O., Sanz-Alonso, D., and Stuart, A. M. Importance sampling: Intrinsic dimension and computational cost. *Statistical Science*, pp. 405–431, 2017. (Cited on page 14)
- Akhound-Sadegh, T., Rector-Brooks, J., Bose, J., Mittal, S., Lemos, P., Liu, C.-H., Sendera, M., Ravanbakhsh, S., Gidel, G., Bengio, Y., Malkin, N., and Tong, A. Iterated denoising energy matching for sampling from boltzmann densities. In Salakhutdinov, R., Kolter, Z., Heller, K., Weller, A., Oliver, N., Scarlett, J., and Berkenkamp, F. (eds.), *Proceedings of the 41st International Conference on Machine Learning*, volume 235 of *Proceedings of Machine Learning Research*, pp. 760–786. PMLR, 21–27 Jul 2024. URL <https://proceedings.mlr.press/v235/akhound-sadegh24a.html>. (Cited on page 2)
- Albergo, M. S. and Vanden-Eijnden, E. Building normalizing flows with stochastic interpolants. *International Conference on Learning Representations (ICLR)*, 2023. (Cited on page 3)
- Albergo, M. S. and Vanden-Eijnden, E. Nets: A non-equilibrium transport sampler, 2024. URL <https://arxiv.org/abs/2410.02711>. (Cited on pages 2, 5, and 13)
- Alexey, D. An image is worth 16x16 words: Transformers for image recognition at scale. In *Proceedings of the 9th International Conference on Learning Representations*, 2021. (Cited on page 4)
- Bose, A. J., Brubaker, M., and Kobzyev, I. Equivariant finite normalizing flows. *arXiv preprint arXiv:2110.08649*, 2021. (Cited on pages 2 and 4)
- Buch, I., Giorgino, T., and De Fabritiis, G. Complete reconstruction of an enzyme-inhibitor binding process by molecular dynamics simulations. *Proceedings of the National Academy of Sciences*, 108(25):10184–10189, 2011. (Cited on page 1)
- Chen, R. T. Q., Rubanova, Y., Bettencourt, J., and Duvenaud, D. K. Neural ordinary differential equations. *Neural*

- Information Processing Systems (NIPS)*, 2018. (Cited on pages 2 and 3)
- Daigavane, A., Vani, B. P., Saremi, S., Kleinhenz, J., and Rackers, J. Jamun: Transferable molecular conformational ensemble generation with walk-jump sampling. *arXiv preprint arXiv:2410.14621*, 2024. (Cited on page 9)
- Deringer, V. L. Modelling and understanding battery materials with machine-learning-driven atomistic simulations. *Journal of Physics: Energy*, 2(4):041003, oct 2020. doi: 10.1088/2515-7655/abb011. URL <https://dx.doi.org/10.1088/2515-7655/abb011>. (Cited on page 1)
- Dibak, M., Klein, L., Krämer, A., and Noé, F. Temperature steerable flows and Boltzmann generators. *Phys. Rev. Res.*, 4:L042005, Oct 2022. doi: 10.1103/PhysRevResearch.4.L042005. (Cited on pages 8 and 19)
- Diez, J. V., Schreiner, M., Engkvist, O., and Olsson, S. Boltzmann priors for implicit transfer operators. *arXiv preprint arXiv:2410.10605*, 2024. (Cited on page 9)
- Dinh, L., Sohl-Dickstein, J., and Bengio, S. Density estimation using Real NVP. *International Conference on Learning Representations (ICLR)*, 2017. (Cited on pages 1 and 3)
- Domingo-Enrich, C., Drozdal, M., Karrer, B., and Chen, R. T. Adjoint matching: Fine-tuning flow and diffusion generative models with memoryless stochastic optimal control. *arXiv preprint arXiv:2409.08861*, 2024. (Cited on pages 16 and 17)
- Doucet, A., De Freitas, N., Gordon, N. J., et al. *Sequential Monte Carlo methods in practice*, volume 1. Springer, 2001. (Cited on pages 2, 4, and 6)
- Eastman, P., Swails, J., Chodera, J. D., McGibbon, R. T., Zhao, Y., Beauchamp, K. A., Wang, L.-P., Simonnet, A. C., Harrigan, M. P., Stern, C. D., et al. Openmm 7: Rapid development of high performance algorithms for molecular dynamics. *PLoS computational biology*, 13(7): e1005659, 2017. (Cited on page 19)
- Esser, P., Kulal, S., Blattmann, A., Entezari, R., Müller, J., Saini, H., Levi, Y., Lorenz, D., Sauer, A., Boesel, F., Podell, D., Dockhorn, T., English, Z., Lacey, K., Goodwin, A., Marek, Y., and Rombach, R. Scaling rectified flow transformers for high-resolution image synthesis, 2024. URL <https://arxiv.org/abs/2403.03206>. (Cited on page 23)
- Fu, X., Xie, T., Rebello, N. J., Olsen, B., and Jaakkola, T. S. Simulate time-integrated coarse-grained molecular dynamics with multi-scale graph networks. *Transactions on Machine Learning Research*, 2023. (Cited on page 9)
- Garcia Satorras, V., Hoogeboom, E., Fuchs, F., Posner, I., and Welling, M. E(n) equivariant normalizing flows. *Neural Information Processing Systems (NeurIPS)*, 2021. (Cited on page 4)
- Grathwohl, W., Chen, R. T. Q., Bettencourt, J., Sutskever, I., and Duvenaud, D. FFJORD: free-form continuous dynamics for scalable reversible generative models. *ICLR*, 2019. (Cited on page 23)
- Hutchinson, M. A stochastic estimator of the trace of the influence matrix for laplacian smoothing splines. *Communications in Statistics - Simulation and Computation*, 19(2):433–450, 1990. doi: 10.1080/03610919008812866. URL <https://doi.org/10.1080/03610919008812866>. (Cited on page 23)
- Jarzynski, C. Nonequilibrium equality for free energy differences. *Phys. Rev. Lett.*, 78:2690–2693, Apr 1997. doi: 10.1103/PhysRevLett.78.2690. URL <https://link.aps.org/doi/10.1103/PhysRevLett.78.2690>. (Cited on page 5)
- Jing, B., Corso, G., Chang, J., Barzilay, R., and Jaakkola, T. Torsional diffusion for molecular conformer generation. *Advances in Neural Information Processing Systems*, 35: 24240–24253, 2022. (Cited on page 8)
- Jing, B., Berger, B., and Jaakkola, T. Alphafold meets flow matching for generating protein ensembles. *arXiv preprint arXiv:2402.04845*, 2024a. (Cited on page 8)
- Jing, B., Stärk, H., Jaakkola, T., and Berger, B. Generative modeling of molecular dynamics trajectories. *arXiv preprint arXiv:2409.17808*, 2024b. (Cited on page 9)
- Karczewski, R., Heinonen, M., and Garg, V. Diffusion models as cartoonists! the curious case of high density regions. *arXiv preprint arXiv:2411.01293*, 2024. (Cited on pages 13, 17, and 18)
- Klein, L. and Noé, F. Transferable boltzmann generators. In *Advances in Neural Information Processing Systems*, 2024. (Cited on pages 6, 7, 8, 19, 20, 23, 25, and 27)
- Klein, L., Foong, A. Y., Fjelde, T. E., Mlodozieniec, B., Brockschmidt, M., Nowozin, S., Noé, F., and Tomioka, R. Timewarp: Transferable acceleration of molecular dynamics by learning time-coarsened dynamics. *Neural Information Processing Systems (NeurIPS)*, 2023a. (Cited on pages 9 and 19)
- Klein, L., Krämer, A., and Noé, F. Equivariant flow matching. *Neural Information Processing Systems (NeurIPS)*, 2023b. (Cited on pages 2 and 8)
- Köhler, J., Klein, L., and Noé, F. Equivariant flows: exact likelihood generative learning for symmetric densities.

- International Conference on Machine Learning (ICML)*, 2020. (Cited on page 4)
- Köhler, J., Krämer, A., and Noé, F. Smooth normalizing flows. In Ranzato, M., Beygelzimer, A., Dauphin, Y., Liang, P., and Vaughan, J. W. (eds.), *Advances in Neural Information Processing Systems*, volume 34, pp. 2796–2809. Curran Associates, Inc., 2021. URL <https://proceedings.neurips.cc/paper/2021/file/167434fa6219316417cd4160c0c5e7d2-Paper.pdf>. (Cited on page 8)
- Köhler, J., Invernizzi, M., De Haan, P., and Noé, F. Rigid body flows for sampling molecular crystal structures. *International Conference on Machine Learning (ICML)*, 2023. (Cited on page 8)
- Lee, H., Pabbaraju, C., Sevekari, A. P., and Risteski, A. Universal approximation using well-conditioned normalizing flows. *Advances in Neural Information Processing Systems*, 34:12700–12711, 2021. (Cited on page 4)
- Lewis, S., Hempel, T., Jiménez Luna, J., Gastegger, M., Xie, Y., Foong, A. Y., García Satorras, V., Abdin, O., Veeling, B. S., Zaporozhets, I., et al. Scalable emulation of protein equilibrium ensembles with generative deep learning. *bioRxiv*, pp. 2024–12, 2024. (Cited on page 8)
- Lindorff-Larsen, K., Piana, S., Dror, R. O., and Shaw, D. E. How fast-folding proteins fold. *Science*, 334(6055):517–520, 2011. (Cited on pages 1, 6, and 19)
- Lipman, Y., Chen, R. T. Q., Ben-Hamu, H., Nickel, M., and Le, M. Flow matching for generative modeling. *International Conference on Learning Representations (ICLR)*, 2023. (Cited on page 3)
- Liu, Q. Rectified flow: A marginal preserving approach to optimal transport. *arXiv preprint arXiv:2209.14577*, 2022. (Cited on page 3)
- Liu, X., Zhang, X., Ma, J., Peng, J., and Liu, Q. InstafLOW: One step is enough for high-quality diffusion-based text-to-image generation, 2024. URL <https://arxiv.org/abs/2309.06380>. (Cited on page 23)
- Loshchilov, I. Decoupled weight decay regularization. *arXiv preprint arXiv:1711.05101*, 2017. (Cited on page 23)
- Máté, B. and Fleuret, F. Learning interpolations between boltzmann densities. *Transactions on Machine Learning Research*, 2023. ISSN 2835-8856. URL <https://openreview.net/forum?id=TH6YrEcbth>. (Cited on page 5)
- Matsumoto, M., Saito, S., and Ohmine, I. Molecular dynamics simulation of the ice nucleation and growth process leading to water freezing. *Nature*, 416(6879):409–413, 2002. (Cited on page 1)
- Midgley, L. I., Stimper, V., Antorán, J., Mathieu, E., Schölkopf, B., and Hernández-Lobato, J. M. SE(3) equivariant augmented coupling flows. *Neural Information Processing Systems (NeurIPS)*, 2023a. (Cited on pages 2, 6, 8, and 22)
- Midgley, L. I., Stimper, V., Simm, G. N., Schölkopf, B., and Hernández-Lobato, J. M. Flow annealed importance sampling bootstrap. *International Conference on Learning Representations (ICLR)*, 2023b. (Cited on pages 6 and 8)
- Neal, R. M. Annealed importance sampling. *Statistics and computing*, 11:125–139, 2001. (Cited on page 5)
- Noé, F., Schütte, C., Vanden-Eijnden, E., Reich, L., and Weikl, T. R. Constructing the equilibrium ensemble of folding pathways from short off-equilibrium simulations. *Proceedings of the National Academy of Sciences*, 106(45):19011–19016, 2009. (Cited on page 1)
- Noé, F., Olsson, S., Köhler, J., and Wu, H. Boltzmann generators: Sampling equilibrium states of many-body systems with deep learning. *Science*, 365(6457):eaaw1147, 2019. (Cited on pages 2, 3, and 8)
- Owen, A. B. *Monte Carlo theory, methods and examples*. <https://artowen.su.domains/mc/>, 2013. (Cited on page 4)
- Papamakarios, G., Pavlakou, T., and Murray, I. Masked autoregressive flow for density estimation. *Advances in neural information processing systems*, 30, 2017. (Cited on page 4)
- Parrinello, M. and Rahman, A. Crystal structure and pair potentials: A molecular-dynamics study. *Physical review letters*, 45(14):1196, 1980. (Cited on page 1)
- Ramachandran, G. N., Ramakrishnan, C., and Sasisekharan, V. Stereochemistry of polypeptide chain configurations. *Journal of Molecular Biology*, pp. 95–99, 1963. (Cited on page 6)
- Rezende, D. and Mohamed, S. Variational inference with normalizing flows. *International Conference on Machine Learning (ICML)*, 2015. (Cited on pages 1 and 3)
- Rizzi, A., Carloni, P., and Parrinello, M. Multimap targeted free energy estimation. *arXiv preprint arXiv:2302.07683*, 2023. (Cited on page 8)
- Satorras, V. G., Hoogeboom, E., and Welling, M. E (n) equivariant graph neural networks. *International Conference on Machine Learning (ICML)*, 2021. (Cited on page 2)

- Schebek, M., Invernizzi, M., Noé, F., and Rogal, J. Efficient mapping of phase diagrams with conditional boltzmann generators. *Machine Learning: Science and Technology*, 2024. (Cited on page 8)
- Schreiner, M., Winther, O., and Olsson, S. Implicit transfer operator learning: Multiple time-resolution models for molecular dynamics. In *Thirty-seventh Conference on Neural Information Processing Systems*, 2023. URL <https://openreview.net/forum?id=1kZx7JiuA2>. (Cited on page 9)
- Skreta, M., Atanackovic, L., Bose, A. J., Tong, A., and Neklyudov, K. The superposition of diffusion models using the $\hat{\pi}$ density estimator. *arXiv preprint arXiv:2412.17762*, 2024. (Cited on pages 13 and 17)
- Teshima, T., Ishikawa, I., Tojo, K., Oono, K., Ikeda, M., and Sugiyama, M. Coupling-based invertible neural networks are universal diffeomorphism approximators. *Advances in Neural Information Processing Systems*, 33:3362–3373, 2020. (Cited on page 4)
- Tong, A., Malkin, N., Huguet, G., Zhang, Y., Rector-Brooks, J., Fatras, K., Wolf, G., and Bengio, Y. Improving and generalizing flow-based generative models with mini-batch optimal transport. *arXiv preprint arXiv:2302.00482*, 2023. (Cited on pages 3 and 23)
- Vargas, F., Padhy, S., Blessing, D., and Nüsken, N. Transport meets variational inference: Controlled Monte Carlo diffusions. *International Conference on Learning Representations (ICLR)*, 2024. (Cited on page 5)
- Wirnsberger, P., Ballard, A. J., Papamakarios, G., Abercrombie, S., Racanière, S., Pritzel, A., Jimenez Rezende, D., and Blundell, C. Targeted free energy estimation via learned mappings. *The Journal of Chemical Physics*, 153 (14):144112, 2020. (Cited on pages 1 and 8)
- Zhai, S., Zhang, R., Nakkiran, P., Berthelot, D., Gu, J., Zheng, H., Chen, T., Bautista, M. A., Jaitly, N., and Susskind, J. Normalizing flows are capable generative models. *arXiv preprint arXiv:2412.06329*, 2024. (Cited on pages 2, 4, and 24)

A. Alternate Paths

A.1. Proposal free Langevin dynamics

We can also modify the Langevin SDE in Eq. 6 to include an additional drift term $\nu_\tau(x_\tau) \in \mathbb{R}^d$ as follows:

$$dx_\tau = -\epsilon_\tau \nabla \mathcal{E}_t(x_\tau) d\tau + \nu_\tau(x_\tau) d\tau + \sqrt{2\epsilon_\tau} dW_\tau.$$

Under perfect drift $\nu_\tau(\tau)$ the log weights do not change and there is no need for correction. For imperfect drift the corresponding coupled ODE time-evolution of log-weights $d \log w_\tau$ needed to apply AIS was derived in NETS (Albergo & Vanden-Eijnden, 2024, Proposition 3):

$$dw_\tau = \nabla \cdot \nu_\tau(x_\tau) d\tau - \nabla \mathcal{E}_\tau(x_\tau) \cdot \nu_\tau(x_\tau) d\tau - \partial_\tau \mathcal{E}_\tau(x_\tau) d\tau.$$

In contrast to learning a drift as done in NETS (Albergo & Vanden-Eijnden, 2024) we now illustrate that a judicious choice of $\nu_\tau(x_\tau)$ eliminates the need to compute the gradient of log-likelihood under the proposal. For instance, we can choose $\nu_\tau(x_\tau) = \epsilon_\tau \nabla \mathcal{E}_\tau(x_\tau) - \epsilon_\tau \nabla \left(\frac{\mathcal{E}(x_\tau)}{k_B T} \right)$, which by straightforward calculation gives the following SDE:

$$\begin{aligned} dx_\tau &= -\epsilon_\tau \nabla \mathcal{E}_t(x_\tau) d\tau + \nu_\tau(x_\tau) d\tau + \sqrt{2\epsilon_\tau} dW_\tau \\ &= -\epsilon_\tau \nabla \left(\frac{\mathcal{E}(x_\tau)}{k_B T} \right) d\tau + \sqrt{2\epsilon_\tau} dW_\tau. \end{aligned} \quad (11)$$

This new SDE greatly simplifies the simulation of samples x_τ as it is independent of the proposal energy $\nabla \mathcal{E}_0(x_\tau) = -\nabla \log p_\theta(x_\tau)$. However, the log weights ODE still requires the computation of the gradient of the proposal energy. The form of Eq. 11 suggests the possibility of massively parallel simulation schemes under a regular normalizing flow and a CNF. However, due to simulation the log weights remains expensive for CNFs due to the need to compute the divergence operator in Eq. 4. Furthermore, while recent advances in divergence-free density estimation via the Itô density estimator (Skreta et al., 2024; Karczewski et al., 2024) might appear attractive we show that the log density under this estimator is necessarily biased and may limit the fidelity of self-normalized importance sampling incurs non-negotiable added bias. For ease of presentation, we present this theoretical investigation in appendix §C.2 and characterize the added bias in Proposition 5. In totality, this limits the application of continuous BG's to only the conventional IS setting, unlike finite flows like TarFlow which can benefit from non-equilibrium transport and AIS.

B. Proofs

B.1. Proof of Proposition 1

Proposition 1. *Given an SE(3)-invariant $\mu_{\text{target}}(x)$ and the noise-adjusted distribution $\mu'_{\text{target}}(x)$. Consider the decomposition of a data sample into its constituent mean-free component, \tilde{x} and center of mass $c \in \mathbb{R}^3$, $x = \tilde{x} + c$, where $c \sim \mu(c)$ and $\mu(c)$ is SO(3)-invariant. Then $\mu_{\text{target}}(\tilde{x}) = \mu'_{\text{target}}(\tilde{x})$ if $\mu'_{\text{target}}(x) = \mu(\tilde{x})\mu(\|c\|)$.*

Proof. We start by noting $x = \tilde{x} + c$ and thus we can construct the target as a marginalization over c

$$\mu_{\text{target}}(\tilde{x}) = \int \mu_{\text{target}}(\tilde{x}, c) dc = \int \mu_{\text{target}}(\tilde{x}|c) \mu(c) dc \quad (12)$$

Now select $\mu(c) = \mu(\|c\|)\mu(\phi)\mu(\psi)$ which gives:

$$\int \mu_{\text{target}}(\tilde{x}|c) \mu(c) dc = \int \mu_{\text{target}}(\tilde{x}|c) \mu(\|c\|) \mu(\phi) \mu(\psi) dc. \quad (13)$$

But the target distribution is SE(3)-invariant and thus this results in the following result,

$$\int \mu_{\text{target}}(\tilde{x}|c) \mu(\|c\|) dc = \int \mu_{\text{target}}(\tilde{x}) \mu(\|c\|) dc = \mu'_{\text{target}}(x). \quad (14)$$

□

B.2. Proof of Lemma 1

We first prove a useful lemma that computes the total variation distance between the original distribution of the normalizing flow p_θ and the truncated distribution \hat{p}_θ before proving the propositions.

Lemma 1. *Let p_θ be a generative and denote $\hat{p}_\theta(x)$ the δ -truncated distribution such that $\hat{p}_\theta(x) := \mathbb{P}(p_\theta(x) \geq \delta)$, for a small $\delta > 0$. Define the constant $\beta = \mathbb{P}(p_\theta(x) < \delta)$ as the event where the truncation occurs. Then the total variation distance between the generative model and its truncated distribution is $TV(p_\theta, \hat{p}_\theta) = \beta$.*

Proof. We begin by first characterizing the total variation distance between flow after correction with importance sampling $p(x)$ with truncated distribution $\hat{p}(x)$. Recall that the truncated distribution is defined as follows:

$$\hat{p}(x) := \mathbb{P}(p(x) \geq \delta) = \frac{p(x)\mathbb{I}\{p(x) \geq \delta\}}{\int \mathbb{I}\{p(x) \geq \delta\}p(x)dx}, \quad (15)$$

where \mathbb{I} is the indicator function. Denote the events $\alpha = \mathbb{P}(X \geq \delta)$ and $\beta = \mathbb{P}(X < \delta)$ for the random variance $X \sim p(x)$. Clearly, $\alpha + \beta = 1$ and $\alpha = \int \mathbb{I}\{\mu(x) \geq \delta\}p(x)dx$. Now consider the total variation distance between these two distributions:

$$TV(p, \hat{p}) = \sup_{\phi \in \Phi} |\mathbb{E}_{x \sim p(x)}[\phi(x)] - \mathbb{E}_{\hat{x} \sim \hat{p}(x)}[\phi(\hat{x})]| = \frac{1}{2} \int |p(x) - \hat{p}(x)|dx. \quad (16)$$

where $\Phi = \{\phi : \|\phi\|_\infty \leq 1\}$. Next we break up the event space into two regions R_1 and R_2 which correspond to the events $p(x) < \delta$ and $p(x) \geq \delta$ respectively. Now consider the total variation distance in the region R_1 whereby construction $\hat{p}(x) = 0$,

$$\frac{1}{2} \int_{R_1} |p(x) - \hat{p}(x)|dx = \frac{1}{2} \int_{R_1} p(x)dx = \frac{\beta}{2}. \quad (17)$$

A similar computation on R_2 gives,

$$\frac{1}{2} \int_{R_2} |p_\theta(x) - \hat{p}_\theta(x)|dx = \frac{1}{2} \int_{R_2} \left| p(x) - \frac{p(x)}{\alpha} \right| dx = \frac{1}{2} \int_{R_2} p(x) \left| 1 - \frac{1}{\alpha} \right| dx = \frac{\alpha(\frac{1}{\alpha} - 1)}{2} = \frac{\beta}{2}, \quad (18)$$

where we exploited the fact that $\hat{p}_\theta(x) = \frac{p_\theta(x)}{\alpha}$ in the first equality and that $\alpha = \int_{R_2} p_\theta(x)dx$ in the second equality. Combining these results we get the full total variation distance:

$$TV(p, \hat{p}) = \frac{1}{2} \int |p(x) - \hat{p}(x)|dx = \frac{1}{2} \int_{R_1} |p(x) - \hat{p}(x)|dx + \frac{1}{2} \int_{R_2} |p(x) - \hat{p}(x)|dx = \beta. \quad (19)$$

Thus the $TV(p, \hat{p}) = \beta$ and 0 in the trivial case where $\alpha = 1$ and the truncated distribution are the same. \square

B.3. Proof of Proposition 3

Proposition 3. *Given an energy threshold $\mathcal{E}(x) > \gamma$, for $\gamma > 0$ large and the resulting truncated target distribution $\hat{\mu}_{\text{target}}(x) := \mathbb{P}\left(\mu_{\text{target}}(x) \geq \frac{\gamma}{\log \hat{\mathcal{Z}}}\right)$. Further, assume that the density of unnormalized importance weights w.r.t. to $\hat{\mu}_{\text{target}}$ is square integrable $(\hat{w}(x))^2 < \infty$. Given a tolerance $\rho = 1/\text{ESS}$ and bias of the original importance sampling estimator in total variation $b = TV(\mu_\theta, \mu_{\text{target}})$, then the γ -truncation threshold with K -samples for $TV(\mu_\theta, \hat{\mu}_{\text{target}})$ is:*

$$\gamma \geq \frac{1}{\lambda} \log \left(\frac{Kb}{12\rho\mathbb{E}[\exp(-\lambda X)]} \right) + \log \hat{\mathcal{Z}}. \quad (10)$$

Proof. We start by recalling a well-known result stating the bias of self-normalized importance sampling found in [Agapiou et al. \(2017, Theorem 2.1\)](#) using K samples from the proposal $\mu(x)$:

$$\sup_{\|\phi\|_\infty \leq 1} |\mathbb{E}[\mu_\theta^K(\phi) - \mu_{\text{target}}(\phi)]| \leq \frac{12\rho}{K}, \quad \rho \approx \frac{K}{\text{ESS}} = \frac{K \sum_j^K w(x^j)^2}{\left(\sum_i^K w(x^i)\right)^2} \quad (20)$$

where the terms $\mu_\theta^K(\phi) = \sum_i^K \bar{w}(x^i)\phi(x^i)$ is the self-normalized importance estimator of μ_{target} with samples drawn according to $x^i \sim p_\theta(x)$ and $\|\phi(x)\| \leq 1$ is a bounded test function.

By truncating using an energy threshold $\mathcal{E}(x) < \gamma$, for a large $\gamma > 0$, we truncate the support of $\mu_{\text{target}}(x)$ by cutting off low probability regions that constitute high-energy configurations. More precisely, we have $\hat{\mu}_{\text{target}} := \mathbb{P}\left(\mu_{\text{target}}(x) \geq \frac{\gamma}{\log \hat{\mathcal{Z}}}\right)$, where $\log \hat{\mathcal{Z}}$ is as defined in Eq. 9. Note that $\hat{\mu}_{\text{target}}(x)$ is absolutely continuous w.r.t. to μ_{target} as the support is contained up to modulo measure zero sets. The importance sampling error incurred by using $\hat{\mu}_{\text{target}}$ can be bounded as follows:

$$\sup_{\|\phi\|_\infty \leq 1} |\mathbb{E}[\mu_\theta^K(\phi) - \mu_{\text{target}}(\phi)]| \leq \sup_{\|\phi\|_\infty \leq 1} |\mathbb{E}[\mu_\theta^K(\phi) - \hat{\mu}_{\text{target}}(\phi)]| + \sup_{\|\phi\|_\infty \leq 1} |\mathbb{E}[\hat{\mu}_{\text{target}}(\phi) - \mu_{\text{target}}(\phi)]| \quad (21)$$

$$\leq \frac{12\hat{\rho}}{K} + \beta_1 \quad (22)$$

$$\leq \frac{12\rho}{K} + \beta_1. \quad (23)$$

The first inequality follows from the triangle inequality. Here we note that $\hat{\rho}$ is the ESS which corresponds to using importance weights computed with respect to the truncated target $\hat{\mu}_{\text{target}}$ rather than μ_{target} . The constant $\beta_1 = \text{TV}(\hat{\mu}_{\text{target}}, \mu_{\text{target}})$ and follows from an application of Lemma 1. Further, note that $\rho \geq \hat{\rho}$ since ESS must increase—and thereby $\hat{\rho}$ decreases—as the distributional overlap between the two distributions decreases. Now observe, $\beta_1 = \mathbb{P}\left(X < \frac{\gamma}{\log \hat{\mathcal{Z}}}\right)$, where samples follow the law $X \sim \hat{\mu}_{\text{target}}(x)$. Then a direct application of Chernoff's inequality gives us $\mathbb{P}\left(X < \frac{\gamma}{\log \hat{\mathcal{Z}}}\right) = \beta_1 \leq \exp\left(\frac{\lambda\gamma}{\log \hat{\mathcal{Z}}}\right) \mathbb{E}[\exp(-\lambda X)]$. Thus the additional bias incurred is,

$$\sup_{\|\phi\|_\infty \leq 1} |\mathbb{E}[\hat{\mu}_\theta^K(\phi) - \mu_{\text{target}}(\phi)]| \leq \frac{12\rho}{K} + \beta_1 \leq \frac{12\rho}{K} + \exp\left(\frac{\lambda\gamma}{\log \hat{\mathcal{Z}}}\right) \mathbb{E}[\exp(-\lambda X)]. \quad (24)$$

Where the term $\mathbb{E}[\exp(-\lambda X)]$ is the moment generating function. Setting $b := \text{TV}(\mu_\theta^K, \mu_{\text{target}})$, then we have

$$\gamma \geq \frac{1}{\lambda} \log \left(\frac{Kb}{12\rho\mathbb{E}[\exp(-\lambda X)]} \right) + \log \hat{\mathcal{Z}}. \quad (25)$$

□

B.4. Proof of Proposition 4

Proposition 4. Assume that the density of the model p_θ after importance sampling μ_θ is absolutely continuous with respect to the target μ_{target} . Further, assume that the density of unnormalized importance weights is square integrable $(w(x))^2 < \infty$. Given a tolerance $\rho = 1/\text{ESS}$ of the original importance sampling estimator under μ_θ and bias of the importance sampling estimator in total variation $b = \text{TV}(\mu_\theta, \mu_{\text{target}})$, then the δ -truncation for the truncated distribution $\hat{p}_\theta(x) := \mathbb{P}(p_\theta(x) \geq \delta)$ threshold with K -samples is:

$$\delta \geq \frac{1}{\lambda} \log \left(\frac{Kb}{12\rho\mathbb{E}[\exp(-\lambda X)]} \right). \quad (26)$$

Proof. We aim to bound the total variation distance $\text{TV}(\hat{\mu}_\theta^K, \mu_{\text{target}})$ of using the truncated distribution $\mathbb{P}(p_\theta(x) > \delta)$ by again recalling the bias of self-normalized importance sampling using K samples from $\mu_\theta(x)$:

$$\sup_{\|\phi\|_\infty \leq 1} |\mathbb{E}[\mu_\theta^K(\phi) - \mu_{\text{target}}(\phi)]| \leq \frac{12\rho}{K}, \quad \rho \approx \frac{K}{\text{ESS}} = \frac{K \sum_j^K w(x^j)^2}{\left(\sum_i^K w(x^i)\right)^2} \quad (27)$$

where the terms $\mu_\theta^K(\phi) = \sum_i^K \bar{w}(x^i)\phi(x^i)$ is the self-normalized importance estimator of μ_{target} with samples drawn according to $x^i \sim p_\theta(x)$ and $\|\phi(x)\| \leq 1$ is a bounded test function. We next characterize the error introduced by using the truncated distribution \hat{p}_θ for importance sampling in place of p_θ by first defining the truncated K -sample self-normalized

importance estimator $\hat{\mu}_\theta^K(\phi) = \sum_j^K \bar{w}(x^j)\phi(x^j)$, where $x^j \sim \hat{p}_\theta(x)$. Specifically, we bound the total variation distance:

$$\text{TV}(\mu_\theta, \hat{\mu}_\theta) = \sup_{\|\phi\|_\infty \leq 1} |\mathbb{E}[\mu_\theta^K(\phi) - \hat{\mu}_\theta^K(\phi)]| \quad (28)$$

$$= \sup_{\|\phi\|_\infty \leq 1} \left| \mathbb{E}_{x^i \sim p_\theta} \left[\sum_{i=1}^K \bar{w}(x^i)\phi(x^i) \right] - \mathbb{E}_{x^j \sim \hat{p}_\theta} \left[\sum_{j=1}^K \bar{w}(x^j)\phi(x^j) \right] \right| \quad (29)$$

$$= \frac{1}{2} \left(\mathbb{E}_{x^i \sim p_\theta} \left[\sum_{i=1}^K \bar{w}(x^i) \right] - \mathbb{E}_{x^j \sim \hat{p}_\theta} \left[\sum_{j=1}^K \bar{w}(x^j) \right] \right) \quad (30)$$

Here in the second equality, we used the fact that the test function is bounded $\|\phi\|_\infty \leq 1$. Next, we apply Lemma 1 and leverage the fact that the self-normalized weights are also bounded and achieve a bound on the total variation distance,

$$\text{TV}(\mu, \hat{\mu}) = \frac{1}{2} \left(\mathbb{E}_{x^i \sim p_\theta} \left[\sum_{i=1}^K \bar{w}(x^i) \right] - \mathbb{E}_{x^j \sim \hat{p}_\theta} \left[\sum_{j=1}^K \bar{w}(x^j) \right] \right) \quad (31)$$

$$= \beta_2, \quad (32)$$

where β_2 is the probability mass $\mathbb{P}(X < \delta)$ when $X \sim p_\theta(x)$. Like previously, the overall error can be bounded using the triangle inequality

$$\sup_{\|\phi\|_\infty \leq 1} |\mathbb{E}[\mu_\theta^K(\phi) - \mu_{\text{target}}(\phi)]| \leq \sup_{\|\phi\|_\infty \leq 1} |\mathbb{E}[\hat{\mu}_\theta^K(\phi) - \mu_{\text{target}}(\phi)]| + \sup_{\|\phi\|_\infty \leq 1} |\mathbb{E}[\mu_\theta^K(\phi) - \hat{\mu}_\theta^K(\phi)]| \quad (33)$$

$$\leq \frac{12\hat{\rho}}{K} + \beta_2 \quad (34)$$

$$\leq \frac{12\rho}{K} + \beta_2. \quad (35)$$

Where the last inequality follows from the same logic as in Proposition 3 where ESS goes up after truncation and therefore $\rho > \hat{\rho}$. A direct application of Chernoff's inequality gives us $\mathbb{P}(X < \delta) = \beta_2 \leq \exp(\lambda\delta)\mathbb{E}[\exp(-\lambda X)]$ where we used the moment generating function of $p_\theta(x)$. Thus the additional bias incurred is,

$$\sup_{\|\phi\|_\infty \leq 1} |\mathbb{E}[\mu_\theta^K(\phi) - \mu_{\text{target}}(\phi)]| \leq \frac{12\rho}{K} + \beta_2 \leq \frac{12\rho}{K} + \exp(\lambda\delta)\mathbb{E}[\exp(-\lambda X)]. \quad (36)$$

Setting $b := \text{TV}(\mu_\theta, \mu_{\text{target}})$ as the bias, then we have

$$\delta \geq \frac{1}{\lambda} \log \left(\frac{Kb}{12\rho\mathbb{E}[\exp(-\lambda X)]} \right). \quad (37)$$

□

C. Itô Filtering

C.1. Flow Matching SDE

As shown in Domingo-Enrich et al. (2024) we can write Flow Matching with Gaussian conditional paths and Diffusion models under a unified SDE framework given a reference flow:

$$x_t = \beta_t x_0 + \alpha_t x_1, \quad (38)$$

where $(\alpha_t)_{t \in [0,1]}, (\beta_t)_{t \in [0,1]}$ are functions such that $\alpha_0 = \beta_1 = 0$ and $\alpha_1 = \beta_0 = 1$. In the specific case of flow matching with linear interpolants that we consider we have:

$$x_t = (1-t)x_0 + tx_1. \quad (39)$$

The unified SDE for both flow matching and continuous-time diffusion models as introduced in [Domingo-Enrich et al. \(2024\)](#) is then:

$$dx_t = \kappa_t x + \left(\frac{\sigma_t^2}{2} + \eta_t \right) \mathfrak{s}(x_t, t) + \sigma_t dW_t, \quad \kappa_t = \frac{\dot{\alpha}_t}{\alpha_t}, \eta_t = \beta_t \left(\frac{\dot{\alpha}_t}{\alpha_t} \beta_t - \dot{\beta}_t \right) \quad (40)$$

where $\mathfrak{s}(x_t, t)$ is the score function estimated by the diffusion model. Thus the flow matching SDE is:

$$dx_t = \left(2f_{t,\theta}(t, x_t) - \frac{x_t}{t} \right) dt + \sigma_t dW_t, \quad \sigma_t = \sqrt{(2(1-t)t)} \quad (41)$$

In fact, the Stein score can be estimated from the output of a velocity field and vice-versa:

$$\nabla \log p_t(x_t) = \frac{tf_{t,\theta}(t, x_t) - x_t}{1-t}, \quad f_{t,\theta}(t, x_t) = \frac{x_t + (1-t)\nabla \log p_t(x_t)}{t} \quad (42)$$

Rewriting Eq. 41 in terms of the score function we get,

$$dx_t = \frac{x_t}{t} + \sigma_t^2 \nabla \log p_t(x_t) + \sigma_t dW_t. \quad (43)$$

C.2. Itô filtering

Proposition 5. Assume that the density of the model p_θ after importance sampling μ_θ is absolutely continuous with respect to the target μ_{target} . Further, assume that the density of unnormalized importance weights is square integrable ($w(x)^2 < \infty$). Let $r(x_0)$ be the Itô density estimator for $\log p_0(x_0)$ of the flow matching SDE:

$$dx_t = \frac{x_t}{t} + \sigma_t^2 \nabla \mathfrak{s}_\theta(t, x_t) + \sigma_t dW_t, \quad \sigma_t = \sqrt{(2(1-t)t)}. \quad (44)$$

Given $\rho = 1/\text{ESS}$, and $\zeta > 0$ which is the weight clipping threshold. Then the additional bias of using the Itô density estimator for importance sampling $\hat{\mu}_{r,\theta}$ with clipping is:

$$\sup_{\|\phi\|_\infty \leq 1} |\mathbb{E} [\mu_{r,\theta}^K(\phi) - \mu_{\text{target}}(\phi)]| \leq \frac{12\rho}{K} + \beta_3 + \beta_4, \quad (45)$$

where $\beta_3 = \text{TV}(\mu_{r,\theta}, \mu_\theta)$ and $\beta_4 = \text{TV}(\mu_{r,\theta}, \hat{\mu}_{r,\theta})$.

We now recall Itô's lemma which states that for a stochastic process,

$$dx_t = f_t(t, x_t) + g_t dW_t, \quad (46)$$

and a smooth function $h : \mathbb{R} \times \mathbb{R}^d \rightarrow \mathbb{R}$ the variation of h as a function of the stochastic SDE can be approximated using a Taylor approximation:

$$dh(t, x_t) = \left(\frac{\partial}{\partial t} h(t, x_t) + \frac{\partial}{\partial x} h(t, x_t)^T f_t(t, x_t) + \frac{1}{2} \sigma_t^2 \Delta_x h(t, x_t) \right) dt + \sigma_t \frac{\partial}{\partial x} h(t, x_t) dW_t. \quad (47)$$

where Δ_x is the Laplacian. We will use Itô's Lemma with $h(t, x_t) := \log p_t(x_t)$ to obtain the Itô density estimator ([Skreta et al., 2024](#); [Karczewski et al., 2024](#)) but for flow models

$$d \log p_t(x_t) = \left(\frac{\partial}{\partial t} \log p_t(x_t) + \frac{\partial}{\partial x} \log p_t(x_t)^T f(t, x_t) + \frac{1}{2} \sigma_t^2 \Delta_x \log p_t(x_t) \right) dt + \sigma_t \frac{\partial}{\partial x} \log p_t(x_t) dW_t, \quad (48)$$

To solve for the change in density over time we can start from the log version of the Fokker-Plank equation:

$$\frac{\partial}{\partial t} \log p_t(x) = -\nabla \cdot (f(t, x)) + \frac{1}{2} \sigma_t^2 \Delta_x \log p_t(x) - \nabla_x \log p_t(x)^T \left(f(t, x) - \frac{1}{2} \sigma_t^2 \nabla_x \log p_t(x) \right) \quad (49)$$

in the general case we end with:

$$d \log p_t(x_t) = \left(-\nabla \cdot (f(t, x_t) - \sigma_t^2 \nabla_x \log p_t(x_t)) + \frac{1}{2} \sigma_t^2 \|\nabla_x \log p_t(x_t)\|^2 \right) dt + \sigma_t \nabla_x \log p_t(x_t)^T dW_t. \quad (50)$$

We now apply this to the flow-matching SDE Eq. 43 written in terms of the score function. In particular, we have,

$$\begin{aligned} d \log p_t(x_t) &= \left(-\nabla \cdot \left(\sigma_t^2 \nabla_x \log p_t(x_t) + \frac{x_t}{t} - \sigma_t^2 \nabla_x \log p_t(x_t) \right) + \frac{1}{2} \sigma_t^2 \|\nabla_x \log p_t(x_t)\|^2 \right) dt \\ &\quad + \sigma_t \nabla_x \log p_t(x_t)^T dW_t \\ d \log p_t(x_t) &= \left(-d/t + \frac{1}{2} \sigma_t^2 \|\nabla_x \log p_t(x_t)\|^2 \right) dt + \sigma_t \nabla_x \log p_t(x_t)^T dW_t. \end{aligned} \quad (51)$$

The above equation makes an implicit assumption that we have access to the actual ground truth score function of $\nabla \log p_t(x_t)$ rather than the estimated one \mathfrak{s}_θ , expressed via the vector field as in Eq. 42. When working with imperfect score estimates we have the following SDE:

$$dx_t = \frac{x_t}{t} + \sigma_t^2 \nabla \mathfrak{s}_\theta(t, x_t) + \sigma_t dW_t. \quad (52)$$

The score estimation error causes a discrepancy in $\log p_t(x_t)$ estimates whose error is captured in the theorem from Kar-czewski et al. (2024)[Theorem 3]:

$$\log r_0(x_0) = \log p_0(x_0) + Y \quad (53)$$

where $\log r_0$ is the bias of the log density starting at time $t = 0$ of the auxiliary process that does not track x_t correctly due to the estimation error of the score. Also, Y is a random variable such that that bias of r_0 is given by:

$$\mathbb{E}[Y] = \underbrace{\frac{1}{2} \mathbb{E}_{t \sim \mathcal{U}(0,1), x_t \sim p_t(x_t)} [\sigma_t^2 \|\mathfrak{s}_\theta(t, x_t) - \nabla \log p_t(x_t)\|^2]}_{\geq 0} \quad (54)$$

Thus the Itô density estimator forms an upper bound to the true log density, i.e. $r_0(x_0) \geq \log p_0(x_0)$. This allows us to form an upper bound on the normalized log weights as an expectation,

$$\begin{aligned} \mathbb{E}_{x_0 \sim p_\theta(x_0)} [\log \bar{w}(x_0)] &= \mathbb{E}_{x_0 \sim p_\theta(x_0)} \left[-\frac{\mathcal{E}(x_0)}{k_B T} - \log p_0(x_0) - C \right] \\ &\leq \mathbb{E}_{x_0 \sim p_\theta(x_0)} \left[-\frac{\mathcal{E}(x_0)}{k_B T} - r_0(x_0) \right], \end{aligned}$$

where C is a constant. We define $\log \bar{w}_r(x_0) := -\frac{\mathcal{E}(x_0)}{k_B T} - r_0(x_0)$ as the new normalized importance weights, module constants. We can now compute the additional bias of self-normalized importance sampling estimator $\mu_{r,\theta}^K$

$$\text{TV}(\mu_{r,\theta}, \mu_\theta) = \sup_{\|\phi\|_\infty \leq 1} |\mathbb{E} [\mu_{r,\theta}^K(\phi) - \mu_\theta^K(\phi)]| \quad (55)$$

$$= \sup_{\|\phi\|_\infty \leq 1} \left| \mathbb{E}_{x^i \sim p_\theta} \left[\sum_{i=1}^K \bar{w}_r(x^i) \phi(x^i) \right] - \mathbb{E}_{x^j \sim p_\theta} \left[\sum_{j=1}^K \bar{w}(x^j) \phi(x^j) \right] \right| \quad (56)$$

$$= \frac{1}{2} \left(\mathbb{E}_{x^i \sim p_\theta} \left[\sum_{i=1}^K \bar{w}_r(x^i) \right] - \mathbb{E}_{x^j \sim p_\theta} \left[\sum_{j=1}^K \bar{w}(x^j) \right] \right) \quad (57)$$

$$= \frac{1}{2} \left(\mathbb{E}_{x^i \sim p_\theta} \left[\sum_{i=1}^K \exp \left(\frac{1}{2} \mathbb{E}_{t \sim \mathcal{U}(0,1), x_t \sim p_t(x_t)} [\sigma_t^2 \|\mathfrak{s}_\theta(t, x_t) - \nabla \log p_t(x_t)\|^2] \right) \right] \right) \quad (58)$$

$$:= \beta_3 \quad (59)$$

The total bias is then

$$\sup_{\|\phi\|_\infty \leq 1} |\mathbb{E} [\mu_{r,\theta}^K(\phi) - \mu_{\text{target}}(\phi)]| \leq \frac{12\rho}{K} + \beta_3. \quad (60)$$

Finally, when clipping weights with $\zeta > 0$ we induce a truncated distribution $\hat{\mu}_{r,\theta}$, i.e. $\hat{r}_0 := \mathbb{P}(r_0 x_0 > \zeta)$. Using Lemma 1 this creates another constant factor that contributes $\text{TV}(\mu_{r,\theta}, \hat{\mu}_{r,\theta}) = \beta_4$ to the overall bias:

$$\sup_{\|\phi\|_\infty \leq 1} |\mathbb{E} [\mu_{r,\theta}^K(\phi) - \mu_{\text{target}}(\phi)]| \leq \frac{12\rho}{K} + \beta_3 + \beta_4. \quad (61)$$

D. Datasets

For all datasets besides ALDP we use a training set of 100k contiguous samples (100ps simulation time) from a single MCMC chain, a validation set of the next 20k contiguous samples, and a test set of 100k uniformly sampled samples from the remaining trajectory. Since these are highly multimodal energy functions, this leaves us with biased training data relative to the Boltzmann distribution. We split trajectories this way to test the model in a challenging and realistic setting — where biased samples from MD exist and we would like to generate more uncorrelated and unbiased samples. We describe the datasets below and present the simulation parameters in Table 4.

Table 4. Overview of simulation parameters

Peptide	Force field	Temperature	Time step
Alanine dipeptide (ALDP)	Amber ff99SBildn	300K	1fs
Trialanine (AL3)	Amber 14	310K	1fs
Alanine tetrapeptide (AL4)	Amber ff99SBildn	300K	1fs
Hexaalanine (AL6)	Amber 14	310K	1fs

Alanine Dipeptide (AD2). For this dataset we use the data and data split from Klein & Noé (2024). Here the training set is purposely biased with an overrepresentation of an underrepresented mode, i.e. the positive φ state. This bias makes it easier to reweight to the target Boltzmann distribution. Alanine Dipeptide consist of one Alanine amino acids, an acetyl group, and an N-methyl group.

Trialanine (AL3) and Hexaalanine (AL6). For the peptides composed of multiple alanine amino acids, we generate MD trajectories using the *OpenMM* library (Eastman et al., 2017). All simulations are conducted in implicit solvent, with the simulation parameters detailed in Table 4. These systems do not include any additional capping groups, such as those present in alanine dipeptide (ALDP) and alanine tetrapeptide (AL4), as they are generated in the same manner as described in Klein et al. (2023a). There are two peptide bonds in alanine tripeptide (AL3) and five in alanine hexapeptide (AL6), resulting in two and five distinct Ramachandran plots, respectively.

Alanine Tetrapeptide (AD4). For this dataset we use the same system setup as in Dibak et al. (2022), but treat all bonds as flexible. The original dataset kept all hydrogen bonds fixed, as the Boltzmann Generator was operating in internal coordinates. The MD simulation to generate the dataset is then performed as described above. Alanine Tetrapeptide consist of three Alanine amino acids, an acetyl group, and an N-methyl group. Therefore, there are four distinct Ramachandran plots.

Chignolin. In addition to the small peptide systems, we also investigate the small protein Chignolin, which consists of ten amino acids. Generating a fully converged all-atom simulation for this system is computationally expensive. Therefore, we use the trajectory provided by (Lindorff-Larsen et al., 2011), which was generated using a specialized supercomputer. In contrast to our other datasets, this simulation was performed in explicit solvent and with a different force field. Since our models do not incorporate additional water molecules, we treat the dataset as if it were in implicit solvent and use the same force field as for the other datasets, namely Amber 14. As a result, the trajectory originates from a slightly different distribution than given by the force-field, likely introducing some bias. Therefore, the task is to generate samples from the equilibrium distribution in implicit solvent while only having access to training data obtained from explicit solvent simulations. As before, we use only the first 100k samples for training. This again highlights the strength of Boltzmann generator based methods, which do not require equilibrium training data. However, it also presents an evaluation challenge, as we lack access to equilibrium samples for the implicit solvent simulation to serve as a reference.

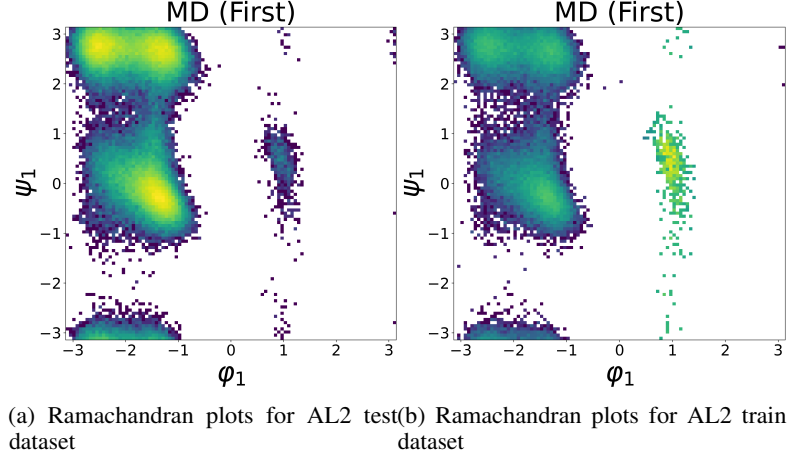


Figure 9. Ramachandran plots for the AL2 dataset with the test (a) and train (b) datasets. We can see that the right mode has been oversampled relative to that of the test set, as in [Klein & Noé \(2024\)](#).

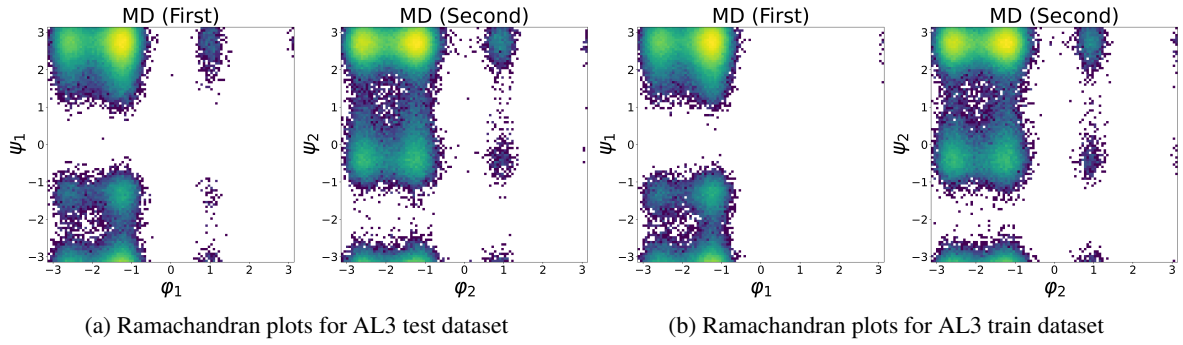


Figure 10. Ramachandran plots for the AL3 test (a) and train (c) histograms over φ and ψ angles. We can see that the training set is completely missing the right mode in ψ_1, φ_1 .

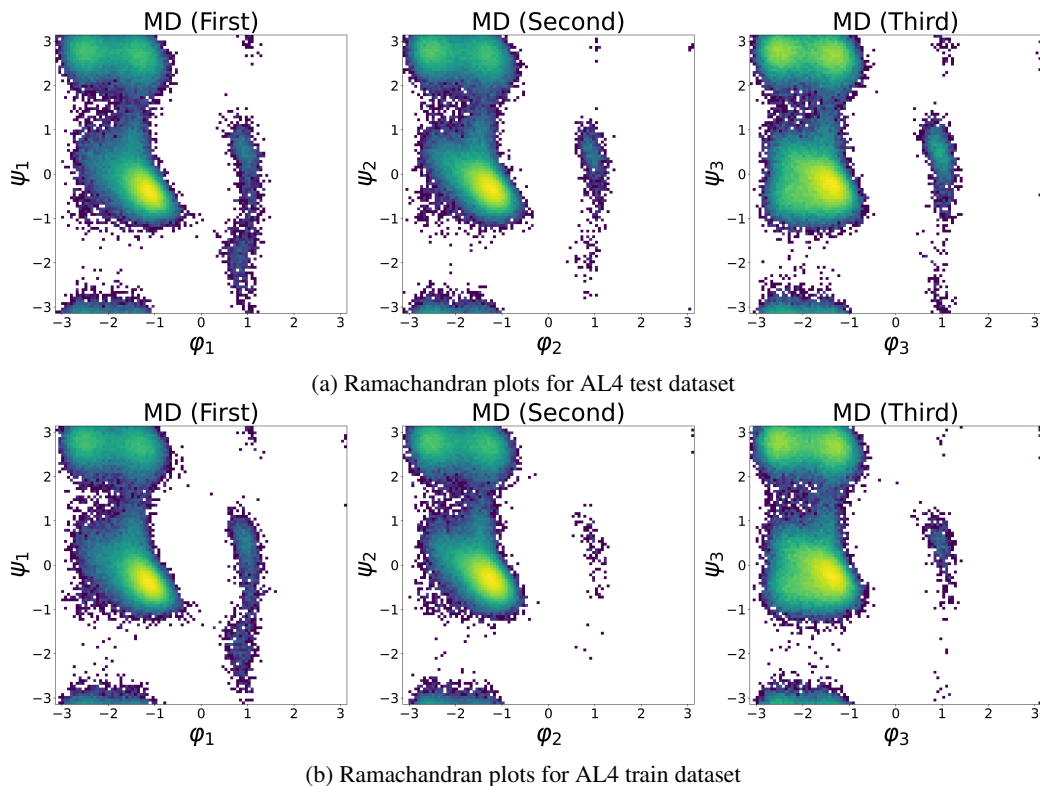


Figure 11. Ramachandran plots for the AL4 dataset with test (a) and training (b) histograms over φ and ψ angles. We can see that the training set is slightly biased with underrepresentation of the small right mode at $\psi_2 \approx 0$ and $\varphi_2 \approx 1$ in the training set as compared to the test set samples.

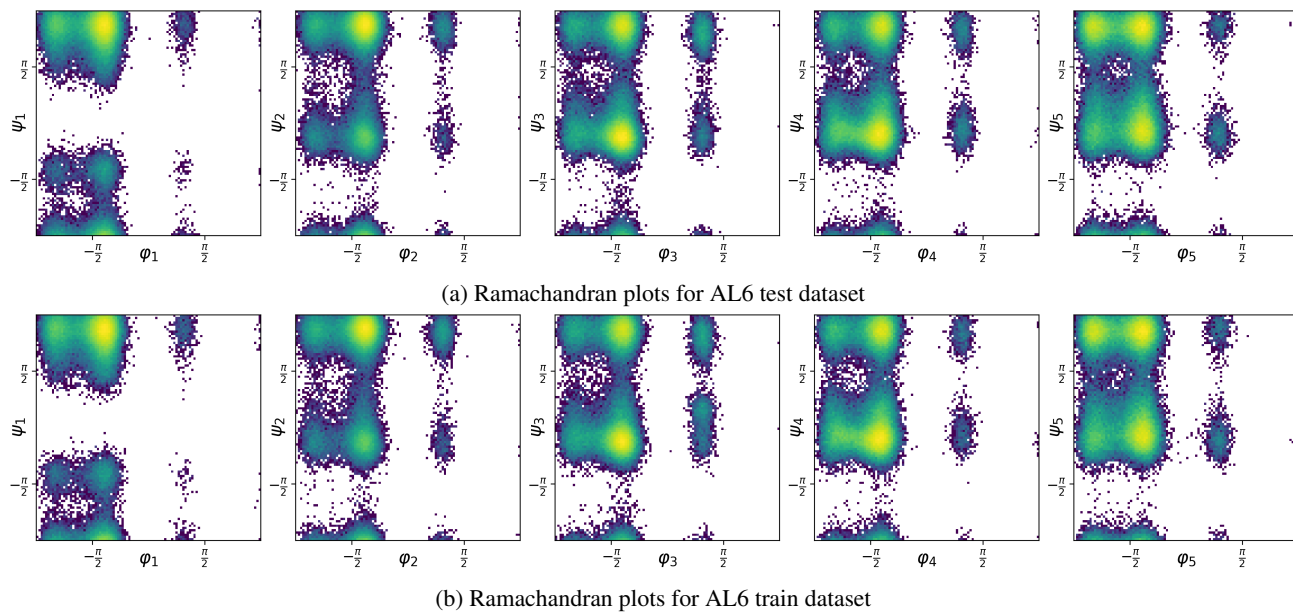


Figure 12. Ramachandran plots for the AL6 dataset with test (a) and training (b) histograms over φ and ψ angles. We can see that the training set has broadly comparable coverage and weighting as the test set for this molecule.

E. Experimental Details

E.1. Metrics and Timings

Metrics and sampling setup. For all metrics we first generate samples, then resample to 10k samples, and finally compute metrics to control for the error in distribution metrics from empirical sample size. For all models we draw 10k samples unless otherwise noted. For AL6 ECNF++ due to compute cost we instead draw 1k samples. For the Torus Wasserstein distance we compute the Wasserstein distance on angle space for the dihedral angles between amino acids. For the vector of φ, ψ which we denote as $(x, y) \in [-\pi, \pi]^{2s}$ where s is the number of dihedral angles. Specifically we compute:

$$\mathbb{T}\text{-}\mathcal{W}_2 = \left(\inf_{\pi} \int c(x, y)^2 d\pi(x, y) \right)^{1/2} \quad (62)$$

where

$$c(x, y) = \left(\sum_i^{2s} ((x_i - y_i) \% \pi)^2 \right)^{1/2} \quad (63)$$

and π represents a coupling between x and y .

Sampling time calculations. For the sampling time, we compute all times on a single A100 80GB, using the maximum power of two batch size possible.

Training time. For training times we compute all times on a single A100 80GB GPU except for SE(3)-EACF which is trained on a single H100. We report the total time in hours until convergence for all methods in the table below.

Table 5. Training time (hours) for all methods.

Model	ALDP	AL3	AL4	AL6	Chignolin
SE(3)-EACF	160	-	-	-	-
ECNF	4.17	5.83	8.89		
ECNF++	9.72	12.5	17.17	76.94	
SBG	16.83	24.67	41.67	57.5	427.33

E.2. SE(3)-EACF Implementation details

Equivariant augmented coupling flow (EACF) (Midgley et al., 2023a). We adopt the original model configuration from (Midgley et al., 2023a) for our EACF baseline on ALDP. Specifically, we choose the more stable spherical-projection EACF with a 20-layer configuration. Each layer has two ShiftCoM layers and two core-transformation blocks. The EGNN used in the core transformation block consists of 3 message-passing layers with 128 hidden states. Stability enhancement tricks like stable MLP and dynamic weight clipping on each layer’s output are fully applied. The model has been trained for 50 epochs with a batch size of 20 using Adam optimizer and peak learning rate of 1×10^{-4} . We use the default 20 samples to estimate likelihoods for importance sampling.

EACF as a Boltzmann generator. EACF is augmented, and therefore to estimate the likelihood of a sample x under an EACF model, we need to use an estimate based on samples from the augmented dimension a . Specifically, for a Gaussian distributed augmented variable a , we can estimate the marginal density of an observation as

$$q(x) = \mathbb{E}_{a \sim \pi(\cdot|x)} \left[\frac{q(x, a)}{\pi(a|x)} \right], \quad (64)$$

however, this is only a consistent estimator of the likelihood and for finite sample sizes has variance. This makes EACF unsuitable for our application of large-scale Boltzmann generators, as in this setting we need to compute exact likelihoods. Variance in likelihood estimation would lead to bias in the final distribution under self-normalized importance sampling or a SBG strategy. We therefore do not consider EACF as a viable option for large scale Boltzmann distribution sampling.

E.3. ECNF Implementation details

E.3.1. NETWORK AND TRAINING

Equivariant continuous normalizing flow (ECNF) (Klein & Noé, 2024). We use the supplied pretrained model from Klein & Noé (2024) for our ECNF baseline on ALDP. Therefore all training parameters are equivalent to, and specified in, that work. We use the specification for the model “TBG+Full” in that work.

ECNF++. We note five improvements to the ECNF, which together substantially improve performance.

1. **Flow matching loss.** In Klein & Noé (2024) a flow matching algorithm with smoothing is employed which provides extra stability during training. This is depicted in Alg. 2, however this smooths out the optimal target distribution (Tong et al., 2023, Proposition 3.3). ECNF uses $\sigma = 0.01$ where we use $\sigma = 0$ for ECNF++. We find that $\sigma > 0$ in this case causes poor molecular structures to be generated as the bond lengths are not able to be controlled precisely enough. We note that $\sigma = 0$ is used in most recent large scale flow matching models (Liu et al., 2024; Esser et al., 2024).
2. **Data normalization strategy.** In previous work, data was normalized to Ångström (Å) scale. We find this to be too small for stable neural network training and instead employ the standard scheme of standardization based on the training data statistics. Specifically, we subtract the center of mass of each atom, and divide by the standard deviation of the data. Typically this would be done with a per-dimension standard deviation. However, to maintain SE(3) equivariance we use a single standard deviation for the whole dataset. On ALDP, the standard deviation of the normalized training data is approximately 0.16, hence we scale up the training data roughly 6-fold on this dataset. We find this greatly improves the training dynamics and final structure precisions.
3. **Architecture size.** Empirically, we find the ECNF to be underparameterized. We perform a grid search over layer width and depth, finding a width of 256 and depth of 5 block to be a good balance between performance and speed on ALDP. We used the same parameters for larger molecular systems.
4. **Improved optimizer and LR scheduler.** We find using an AdamW (Loshchilov, 2017) with fairly large weight decay improves performance and stability. Prior work has found weight decay helps to keep the Lipschitz constant of the flow low and avoids stiff dynamics which enables accurate ODE solving during inference. We also use a smoothly varying cosine schedule with warmup (over 5% of iteration budget) which enables a larger maximum learning rate and faster training than the two step schedule used previously. Both the start and end learning rates are 500 times lower than the defined maximum.
5. **Exponential moving average.** We use an exponential moving average (EMA) on the weights with decay 0.999. This is standard practice in flow models, which improves performance.

These five elements together greatly improve the ECNF training and provide a strong foundation for future Boltzmann generator training on molecular systems using equivariant continuous normalizing flows. Qualitatively, we find ECNFs quite stable to train and robust to training parameters relative to invertible architectures. However, it is very slow to compute the exact likelihood which is necessary for importance sampling.

Other parameters. For both models we use Adam default optimizer parameters for $\beta_1, \beta_2, \epsilon$. For inference we use a Dormand-Prince 45 (dopri5) adaptive step size solver with absolute tolerance 10^{-4} and relative tolerance 10^{-4} .

Likelihood evaluation. Evaluating the likelihood of a CNF model requires calculating the integral of the divergence, as in Eq. 2. While there exist fast unbiased approximations of the likelihood using Hutchinson’s trace estimator (Hutchinson, 1990; Grathwohl et al., 2019), these are unfortunately unsuitable for Boltzmann generator applications where variance in the likelihood estimator leads to biased weights under self-normalized importance sampling. We therefore calculate the Jacobian using automatic differentiation which is both memory and time intensive. For example, on AL6, the maximum batch size that can fit on an 80GB A100 GPU is 8. This batch takes around 2 minutes for 84 integration steps. We also use an improved vectorized Jacobian trace implementation for all CNF which reduces memory by roughly half and time by roughly 3x over previous implementations. We note that these numbers are approximate and depend heavily on both the batch size and the input dimensions.

On using a CNF proposal with SBG. In principle it is possible to drop in replace our NF architecture with a CNF in SBG. However, there are several drawbacks to such an approach, most notably in efficiency. As previously discussed, CNFs are

Algorithm 2 ECNF flow matching training

Input: Prior q_0 , Empirical samples from data q_1 , bandwidth σ , batchsize b , initial network v_θ .

while Training **do**

$\mathbf{x}_0 \sim q_0(\mathbf{x}_0)$; $\mathbf{x}_1 \sim q_1(\mathbf{x}_1)$ {Sample batches of size b i.i.d. from the dataset}

$t \sim \mathcal{U}(0, 1)$

$\mu_t \leftarrow t\mathbf{x}_1 + (1 - t)\mathbf{x}_0$

$x \sim \mathcal{N}(\mu_t, \sigma^2 I)$

$\mathcal{L}(\theta) \leftarrow \|v_\theta(t, x) - (\mathbf{x}_1 - \mathbf{x}_0)\|^2$

$\theta \leftarrow \text{Update}(\theta, \nabla_\theta \mathcal{L}(\theta))$

end while

Return v_θ

extremely computationally inefficient to sample a likelihood from. We find on the order of 100 SBG steps are necessary for best performance. This would make CNFs at least two orders of magnitude slower to sample from, when they are already at the edge of tractability for the current importance sampling estimates. We leave it to future work to consider faster CNF likelihoods and note that our SBG algorithm could be applied there readily.

E.4. Sequential Boltzmann generators implementation details

Architecture. We scale the TarFlow architecture for increasingly challenging datasets. As advised by Zhai et al. (2024) we scale the layers per block alongside the number of blocks. The layers / blocks / channels and resulting number of parameters are presented in Table 6. We note the larger number of parameters in the TarFlow relative to the ECNF++ despite the faster inference walltime, due to the lack of simulation and higher computational efficiency of the architecture.

Table 6. TarFlow configurations across different datasets

Dataset	Layers per Block	Number Blocks	Channels	Number Parameters (M)
ALDP	4	4	256	12.7
AL3	6	6	256	28.5
AL4	6	6	384	64.0
AL6	6	6	384	64.0
Chignolin	8	8	512	202.0

Training configuration. The training hyperparameters used closely follow those of Zhai et al. (2024), although we deviate in using a larger value of weight decay as instability was observed during training. Namely we use a learning rate of 1×10^{-4} , weight decay of 4×10^{-4} , Adam β_1, β_2 of (0.90, 0.95) and Adam ϵ of 1×10^{-8} . We additionally employ the same cosine decay learning rate schedule with warmup (start and end learning rate 500 times lower than maximum value) and exponential moving average decay (0.999) used in ECNF++. Training is performed for 1000 epochs. As non-monotonic improvement was observed on validation metrics, we use early stopping based on the $\mathcal{E}\text{-}\mathcal{W}_1$ against the validation dataset, where the proposal p_θ was cropped to a target energy range of interest to ignore outlier samples that will be removed by energy cropping during inference.

Sampling hyperparameters. Whilst the TarFlow is capable of generating low-energy peptide states, it is also prone to generating samples of extremely high target energy. For standard importance sampling this presents no issue as these samples will be assigned importance weights of approximately 0. However, for the SBG these high energy samples were prone to numerical instability during Langevin dynamics. To mitigate this issue we truncate the proposal distribution prior p_θ based on an energy cutoff, noting that the bias introduced by this operation is bounded in Proposition 3. Similarly to EACF, we additionally remove the samples corresponding to the largest 0.2% of importance weights, in the case of SBG this is performed once, prior to Langevin dynamics. See §F.3 for an ablation on the effect of weight clipping in SBG. For ALDP, AL3, AL4 and AL6 we use 100 Langevin timesteps for our main results, with $\epsilon = 1 \times 10^{-5}$ and $\text{ESS}_{\text{threshold}} = 0.5$. For Chignolin we use 100 timesteps, with $\epsilon = 1 \times 10^{-9}$ and $\text{ESS}_{\text{threshold}} = 0.99$. For ablations of these hyperparameters see §F.3. Simple multinomial resampling is used for all datasets except Chignolin where stratified resampling is used.

Table 7. Overview of training configurations

Training Parameter	ECNF	ECNF++	TarFlow
Optimizer	Adam	AdamW	AdamW
Learning Rate	5×10^{-4}	5×10^{-4}	1×10^{-4}
Weight Decay	0.0	1×10^{-2}	4×10^{-4}
$\beta_1, \beta_2, \varepsilon$	h0.9, 0.999, 1e-8	0.9, 0.999, 1e-8	0.9, 0.95, 1e-8
EMA Decay	0.000	0.999	0.999
Width	64	256	Varies
N blocks	5	5	Varies
Parameters	152 K	2.317 M	Varies

F. Additional Results

F.1. Chirality

The ECNF architecture is E(3) equivariant, hence is equivariant to reflections, and will generate samples of both possible global chiralities. As the energy functions are themselves invariant to reflections this is not resolved by importance sampling. Having the correct global chirality is necessary to match the test dataset dihedral angle distributions where only one global chirality is present in the data. The incorrect chirality can show up as a symmetric mode on Ramachandran plots. To resolve this issue we follow Klein & Noé (2024) in detecting incorrect chirality conformations, and reflecting them. Points with unresolvable symmetry (e.g mixed chirality conformations) are dropped. The results for $\mathbb{T}\text{-}\mathcal{W}_2$ before and after fixed-chirality samples are presented in Table 8. We observe a reduction in metric value (improved performance) on all configurations aside from ECNF AL4, which we attribute to evaluation noise. We further note that non-equivariant methods such as SBG do not suffer this effect and hence do not require any symmetry post-processing.

 Table 8. $\mathbb{T}\text{-}\mathcal{W}_2$ results for unprocessed and fixed-chirality samples from ECNF and ECNF++

Datasets \rightarrow	Tripeptide (AL3)		Tetrapeptide (AL4)		Hexapeptide (AL6)	
Algorithm \downarrow	Unprocessed	Fixed	Unprocessed	Fixed	Unprocessed	Fixed
ECNF	7.010	4.241	3.853	4.902	-	-
ECNF++ (Ours)	1.967 ± 0.062	1.177 ± 0.145	2.414 ± 0.000	2.082 ± 0.005	5.405 ± 0.069	4.315 ± 0.018

F.2. Ramachandran Plots

In this appendix we include the Ramachandran plots for each model on each peptide. Please note that the ground truth training and test Ramachandran plots are located in Appendix D.

Alanine dipeptide (ALDP). In Figure 13 we present the Ramachandran plot for ALDP. We find that that ECNF++ models the distribution well, but drops the positive φ mode. Which is quite interesting as this mode is oversampled in the training data (see Figure 9).

Trialanine (AL3). In Figure 14 we can see the Ramachandran plot for resampled points for the Trialanine dataset. Comparing this to the train and test data in Figure 10 we see that the AL3 training data is missing the φ_1 positive mode which is reflected in all of the models. We find that our SBG model is able to best capture the low density modes, although barely captures the lowest density mode in the second peptide bond.

Alanine tetrapeptide (AL4). In Figure 16 we can see the Ramachandran plot for resampled points for the Trialanine dataset. Comparing this to the train and test distributions in Figure 11 we observe that both ECNF++ and SBG capture the dihedral angle distribution with comparable success, although the ECNF++ has very few points in the positive φ modes. This is to be expected give the relatively small improvement of $\mathbb{T}\text{-}\mathcal{W}_2$ seen in Table 3 for this dataset.

Hexaalanine (AL6). In Figure 16 we present the Ramchandran plots for samples from ECNF++ and SBG. Due to computational constraints only 1,000 samples are plotted for ECNF++, whereas 100,000 are present for SBG. With so few samples for ECNF++ it is not possible to compare methods. We find that SBG succeeds to capture the low density positive

φ modes, albeit with a tight concentration of points as opposed to a broad range of low density. We additionally observe the negative Ψ_1 mode to be well captured by the SBG.

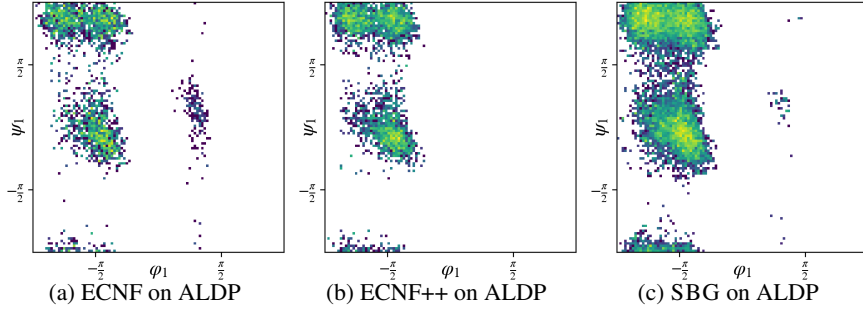


Figure 13. Alanine dipeptide (ALDP) Ramachandran plots. 10,000 points plotted for ECNF++, 100,000 points plotted for SBG.

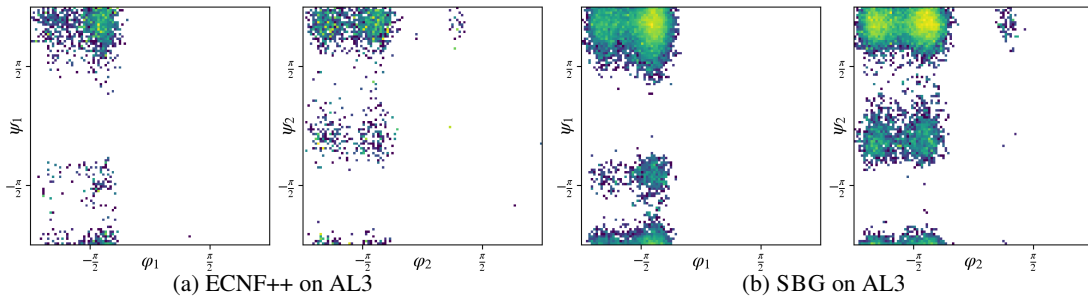


Figure 14. Trialanine (AL3) Ramachandran plots. 10,000 points for ECNF++, 100,000 points for SBG.

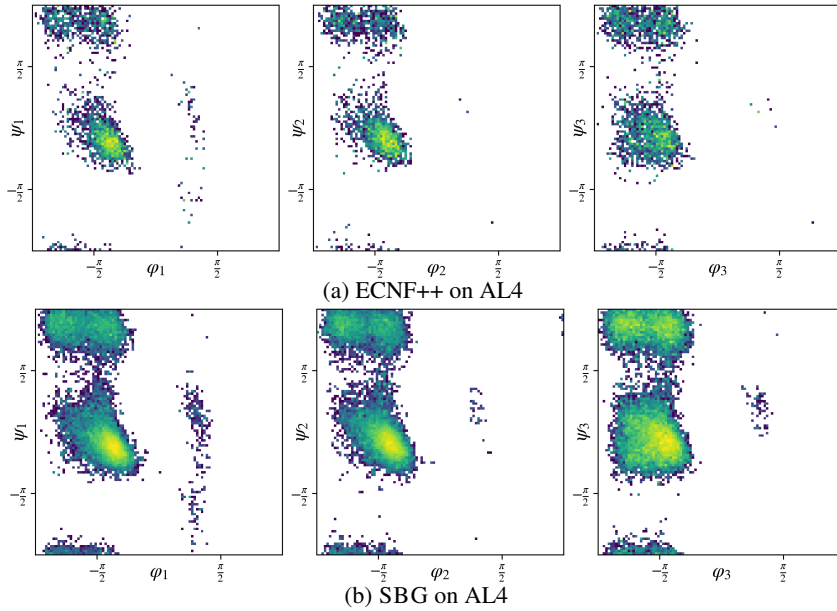


Figure 15. Alanine tetrapeptide (AL4) Ramachandran plots. 10,000 points plotted for ECNF(++), 100,000 points plotted for SBG.

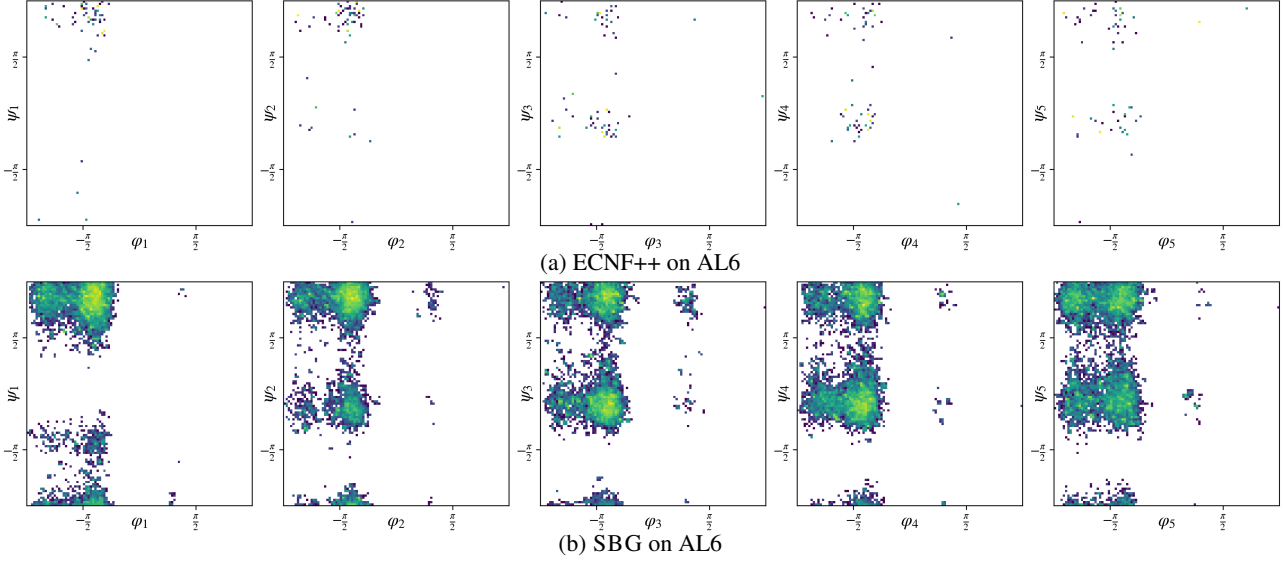


Figure 16. Ramachandran plots for various models on AL6 dataset. Due to computational constraints only 1,000 points plotted for ECNF++, 100,000 points plotted for SBG.

F.3. Ablation studies

Ablation of IS and SMC. In Table 9 we compare the quantitative performance of the TarFlow on AL3 without reweighting (Proposal), with standard importance sampling (BG) and with Annealed Langevin SMC (SBG). We observe a dramatic reduction in $\mathcal{E}\text{-}\mathcal{W}_1$ for the BG over the proposal, with a strong further decrease for SBG on AL3 and AL6. On ALDP $\mathbb{T}\text{-}\mathcal{W}_2$ improves greatly when reweighting, which is expected as the training data and subsequently the proposal distribution was intentionally biased to provide improved coverage (Klein & Noé, 2024). On the other datasets the reweighting moderately increases the $\mathbb{T}\text{-}\mathcal{W}_2$, with little distinction between the reweighting methods.

Table 9. Quantitative results comparing (unweighted) proposal, Boltzmann generator (BG) and sequential Boltzmann generator (SBG).

Datasets →	Alanine dipeptide (ALDP)		Tripeptide (AL3)		Tetrapeptide (AL4)		Hexapeptide (AL6)	
Model	$\mathcal{E}\text{-}\mathcal{W}_1 \downarrow$	$\mathbb{T}\text{-}\mathcal{W}_2$	$\mathcal{E}\text{-}\mathcal{W}_1 \downarrow$	$\mathbb{T}\text{-}\mathcal{W}_2$	$\mathcal{E}\text{-}\mathcal{W}_1 \downarrow$	$\mathbb{T}\text{-}\mathcal{W}_2$	$\mathcal{E}\text{-}\mathcal{W}_1 \downarrow$	$\mathbb{T}\text{-}\mathcal{W}_2$
Proposal	9.416 ± 0.575	1.139 ± 0.013	5.873 ± 0.426	0.754 ± 0.013	5.714 ± 0.361	1.716 ± 0.015	45.190	2.923
BG	0.455 ± 0.395	0.225 ± 0.014	1.862 ± 0.431	0.949 ± 0.065	2.028 ± 0.317	1.861 ± 0.039	0.889	3.432
SBG	0.466 ± 0.380	0.226 ± 0.029	1.314 ± 0.409	0.948 ± 0.068	1.920 ± 0.251	1.841 ± 0.047	0.305	3.326

Center of mass adjusted energy. As discussed in §3.1, the TarFlow proposal distribution is not mean-free due to the CoM data augmentation applied to the training data, with a centroid norm distribution $\|C\| \sim \sigma\chi_3$. This can introduce adverse behavior, as the target energy is invariant to $\|C\|$, and thus the importance weights $p(x)/p_\theta(x)$ will depend on $\|C\|$ of a sample x . Concretely, a low (target) energy sample generated far from the origin (with large $\|C\|$) will have low likelihood under p_θ but high likelihood under p leading to a very large importance weight.

To provide a visual intuition for this effect, we plot in Figure 17 the centroid norm distribution of the TarFlow proposal samples before and after (standard) importance sampling (e.g a BG with TarFlow proposal). Here the empirical distribution is generated using 2×10^7 samples, to approximate the asymptotic behavior. In Figure 17a we observe that, even with this large number of samples, without weight clipping or CoM adjusted energy (Equation (5)) the $\|C\|$ distribution is greatly influenced by the reweighting. In this case resampling transports most density to high $\|C\|$ samples, where there was very little density prior to reweighting and hence little sample diversity, and a large peak manifests resulting from a single sample with very large importance weight. In contrast, in Figure 17b we see a much smaller change in $\|C\|$ distribution after reweighting, with no large peak for any given sample, after applying the CoM adjustment. In this case there is no overweighting of high $\|C\|$ regions with limited sample diversity. Adding weight clipping to the standard proposal energy function (Figure 17c) greatly reduces the change in distribution from reweighting, although the mean remains notably shifted

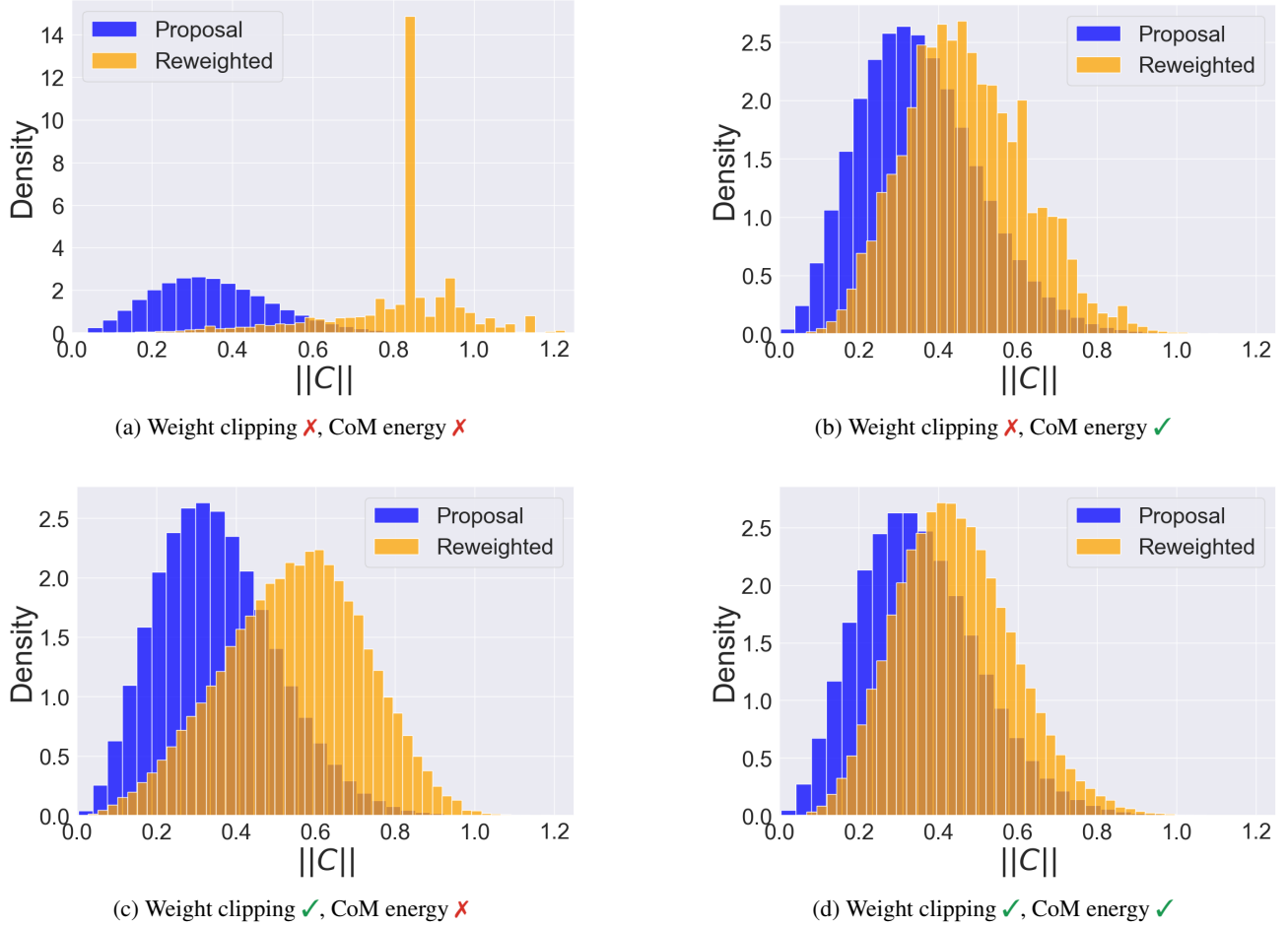


Figure 17. Centroid norm $\|C\|$ histograms for 2×10^7 proposal samples and reweighted proposal samples, with / without both of weight clipping (0.2%) and center of mass adjusted energy.

towards higher $\|C\|$ samples. Applying weight clipping with the CoM adjusted proposal energy function (Figure 17d) has little effect on the $\|C\|$ distribution beyond smoothing. We emphasize that these plots are presented for 2×10^7 samples hence clipping may have a larger still effect for both proposal energy functions for smaller sample sets.

In Figures 18 and 19 we ablate the utility of performing the center of mass energy adjustment to the proposal energy. Specifically, we ablate the CoM adjustment as a function of number of samples used during inference and also as a function of a number of inference timesteps. Each of these ablations is performed on the trialanine tripeptide (AL3). Considering Figure 18, there is little distinction between variants on $\mathcal{E}\text{-}\mathcal{W}_1$ with respect to N samples, although standard energy without clipping can be identified as the least performant, and all methods improve with increased N . On $\mathbb{T}\text{-}\mathcal{W}_2$ the standard energy without clipping is again evidently the worst performing, with a clear benefit to applying the CoM adjustment where clipping is not used. The best performing variants do employ clipping, with a slight but clear benefit to using the CoM adjustment. Considering Figure 19, we observe that, with clipping, the standard energy is more performant on $\mathcal{E}\text{-}\mathcal{W}_1$, however for sufficient timesteps the non-clipped CoM energy is the most performant. On $\mathbb{T}\text{-}\mathcal{W}_2$ the clipped variants are much more performant at low timestep budgets, although the non-clipped CoM asymptotically achieves comparable values. CoM energy with clipping slightly improves with timesteps whereas standard energy with clipping actually diverges. The non-clipped standard energy is least performant on both metrics for almost all timesteps.

Resampling threshold. In Figure 20 we ablate the resampling threshold (using the CoM energy with clipping as in our main experiments). We observe no clear trend in performance with respect to this hyperparameter with many unstable values, particularly near the boundaries, and a stable range around the value 0.5.

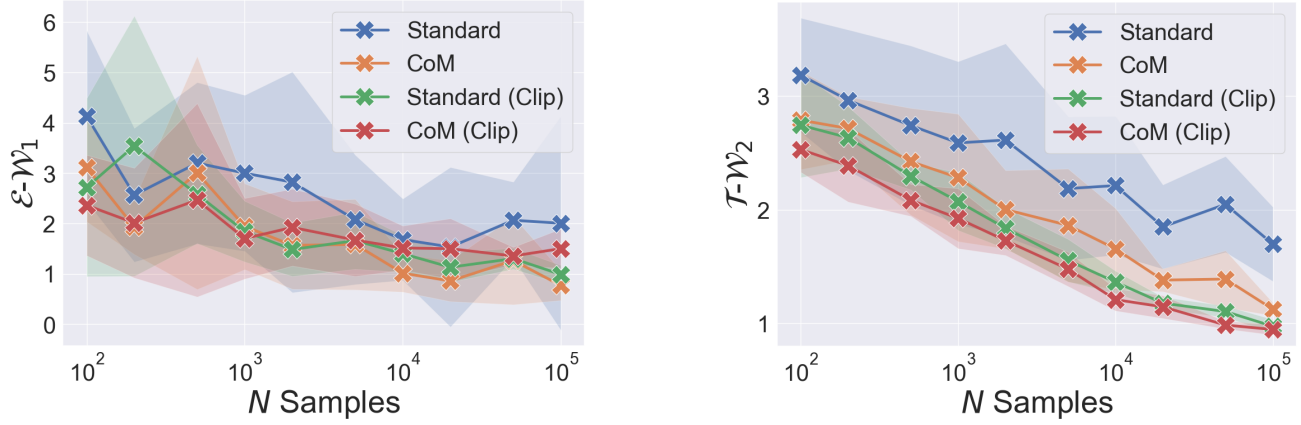


Figure 18. Energy Wasserstein-1 and dihedral angle Wasserstein-2 performance of standard and center of mass adjusted energy, with / without weight clipping (0.2%) at a variety of sampling set sizes.

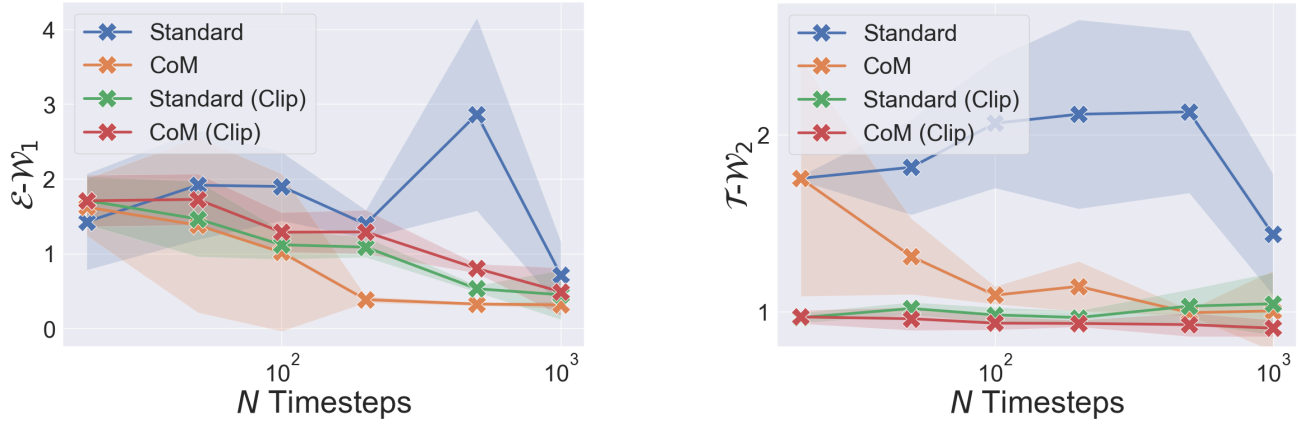


Figure 19. Energy Wasserstein-1 and dihedral angle Wasserstein-2 performance of SBG on AL3 with respect to Langevin time discretization.

Ablation on EACF Importance Weight Clipping. We report the additional results on EACF trained on ALDP dataset. We chose to use 0.2% clip threshold on the importance weights for fair comparison. Nevertheless, in the resampling process, we observe a significant degradation in sample diversity, as evidenced by the energy histograms and Rama plots. From the qualitative results in Figure 21, we can see that EACF generates highly unreliable importance weights, particularly visible in the energy histograms where there are extreme spikes and poor alignment with the true data distribution. This leads to poor resampling quality, as demonstrated in the corresponding Rama plots where the resampled points fail to capture the true data distribution. While increasing the clipping threshold to 10% shows some improvement, the fundamental issue of inaccurate importance weight estimation by EACF persists across different clipping ratios.

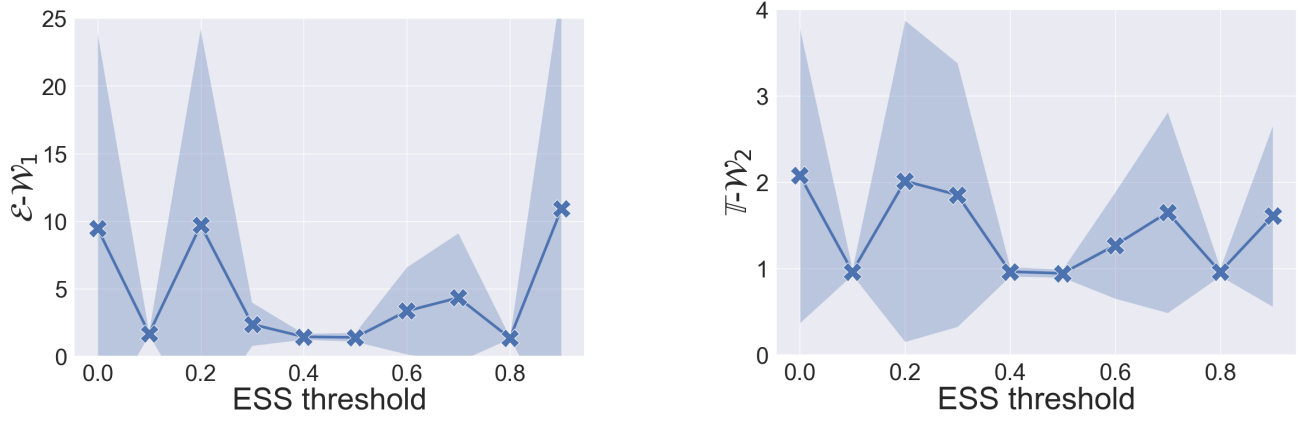


Figure 20. Energy Wasserstein-1 and dihedral angle Wasserstein-2 performance of SBG on AL3 with respect to ESS threshold.

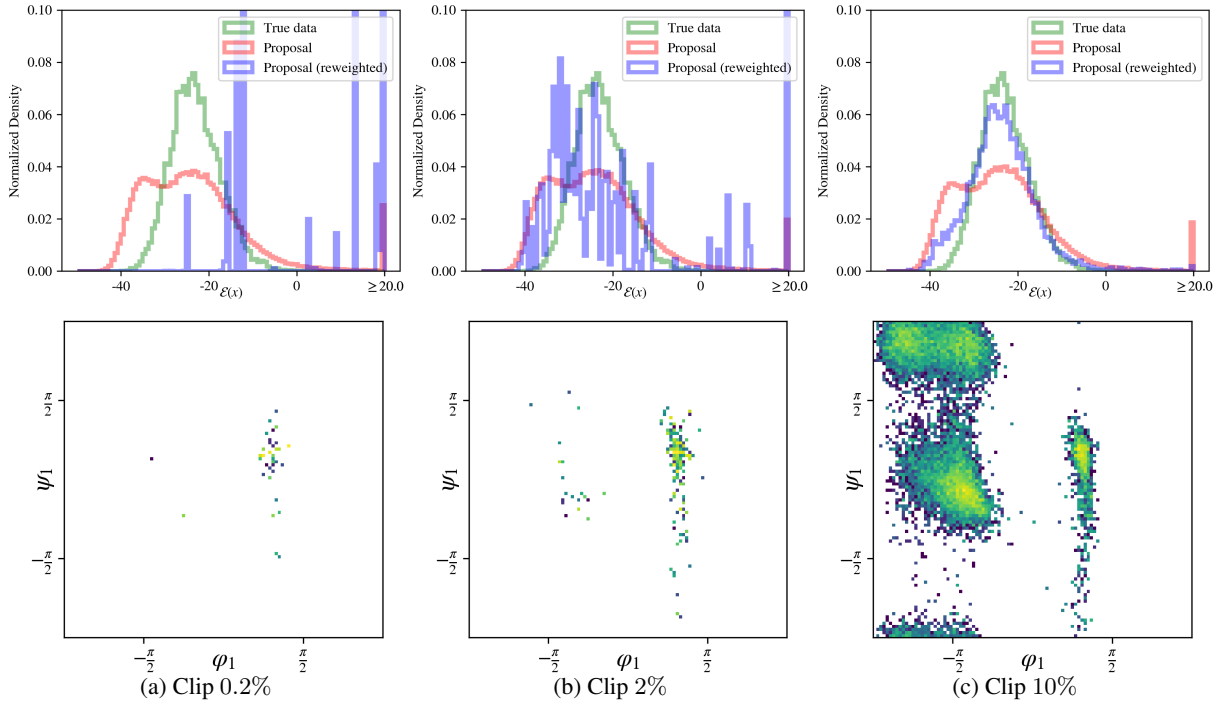


Figure 21. Energy histogram and Ramachandran Plots of EACF under different clipping ratio [0.2%, 2%, 10%].